Available online at www.sciencedirect.com
ScienceDirect
Comput. Methods Appl. Mech. Engrg. 377 (2021) 113704
Computer methods in applied mechanics and engineering
www.elsevier.com/locate/cma

Non-convolutional second-order complex-frequency-shifted perfectly matched layers for transient elastic wave propagation

Stijn François[a], Heedong Goh[b], Loukas F. Kallivokas[b,c,*]

[a] Department of Civil Engineering, KU Leuven, Leuven, Belgium
[b] Department of Civil, Architectural and Environmental Engineering, The University of Texas at Austin, Austin, TX, USA
[c] Oden Institute for Computational Engineering and Sciences, The University of Texas at Austin, Austin, TX, USA

Received 4 November 2020; received in revised form 19 January 2021; accepted 24 January 2021
Available online xxxx

Abstract

The numerical simulation of wave propagation in heterogeneous unbounded media using domain discretization techniques requires truncation of the physical domain: at the truncation boundary, Perfectly Matched Layers (PMLs) – buffers wherein wave attenuation is imposed – are often used to mimic outgoing wave motion and prevent waves from re-entering the interior computational domain. The PML's wave-dissipative properties derive from a coordinate mapping concept, where the physical coordinate is mapped onto a frequency-dependent complex coordinate in the PML via a complex stretching function. The choice of the stretching function controls not only the spectral character and the absorptive properties of the PML, but also, more critically, the long-time stability when the computational domain-PML ensemble is used for transient wave simulations.

The standard PML stretching function can lead to error growth, particularly when propagating waves impinge at grazing incidence on the truncation boundary. By contrast, a modification to the standard stretching function that has led to the Complex-Frequency-Shifted CFS-PML has been shown to alleviate the temporal instability. However, whereas PML formulations using the standard stretching function can lead to second-order in time semi-discrete forms, affording multifaceted benefits, all CFS-PML formulations to date require the evaluation of convolutions. In this paper, we discuss a new CFS-PML formulation that avoids the evaluation of convolutions, while preserving the second-order temporal character of elastic waves. It is shown that, upon spatial discretization, the CFS-PML can be completely described by a triad of stiffness, damping, and mass matrices, which can be readily incorporated into existing finite element codes originally designed for interior problems, to endow them with wave simulation capabilities on unbounded domains. Numerical experiments in the time-domain demonstrate the efficacy of the proposed approach; we also report long-time stability for problems involving waveguides and grazing wave incidence.

Keywords: Elastodynamics; Wave propagation; Perfectly matched layers; Multi-field finite elements; Unsplit-field non-convolutional CFS-PML

1. Introduction

The numerical simulation of elastic wave propagation in arbitrarily heterogeneous unbounded media is computationally challenging: the central difficulties stem from the material heterogeneity and the need to satisfy

* Corresponding author at: Department of Civil, Architectural and Environmental Engineering, The University of Texas at Austin, Austin, TX, USA.
E-mail addresses: stijn.francois@kuleuven.be (S. François), heedong.goh@utexas.edu (H. Goh), loukas@mail.utexas.edu (L.F. Kallivokas).

https://doi.org/10.1016/j.cma.2021.113704
0045-7825/

Sommerfeld–Kupradze's radiation conditions at infinity [1–5]. For homogeneous domains, boundary element approaches, which benefit from the fact that the Green's functions satisfy by construction the radiation conditions, offer, possibly, the most elegant, albeit not necessarily the most efficient, way to model elastic wave motion in unbounded domains. However, in the presence of heterogeneity, domain discretization methods (and their surrogates) offer the only modeling path. Their use necessitates the truncation of the unbounded physical domain in order to make the computational domain finite. Such truncation introduces artificial, non-physical, boundaries that require special treatment to prevent spurious reflections from the waves impinging on the truncation boundary.

Techniques to render the truncation boundary transparent, reflectionless, or absorptive to the traveling waves could be broadly divided into two categories: methods that attempt to approximate the exact (transparent) condition on the truncation boundary, and methods that introduce a buffer past the truncation boundary, wherein wave decay is enforced. Both non-local and local treatments have been proposed for the former category: a non-local treatment refers to implementations of the exact Dirichlet-to-Neumann (DtN) truncation condition, and a local treatment refers to approximations of the exact DtN, which may relax either the DtN's spatial non-locality, its temporal non-locality, or both. The literature addressing issues and refinements related to either exact or approximate DtN implementations is vast and covers acoustic, electromagnetic, and, the more onerous, elastic waves in both the frequency- and the time-domains; invariably, however, all such attempts we are aware of suffer from the "curse" of homogeneity, and a breakthrough to extend developments to the all-important heterogeneous case is unlikely.

Developments in the second category – the buffer zone approach – are fewer and far apart. One of the earliest developments is the sponge layers proposed by Israeli and Orszag [6]; it was not until the pioneering idea of Bérenger [7], cast first for electromagnetic waves, that the buffer approach to wave absorption gained renewed attention. Bérenger's approach gave birth to the Perfectly-Matched-Layer (PML) – an absorptive buffer zone – where waves are forced to decay, and whose interface with the interior domain (the truncation boundary) is "perfectly" matched, allowing, theoretically, for reflectionless propagation into the buffer zone at all angles of incidence and for all frequencies. To date, the PMLs remain the only viable strategy for numerically simulating wave propagation in arbitrarily heterogeneous domains.

In [8], the authors showed that the PML can be constructed by mapping the physical coordinate along the direction perpendicular to the truncation boundary (interface between the interior domain and the PML buffer) onto a complex coordinate, using a frequency-dependent, complex-valued, so-called, stretching function. It should be noted that the complex coordinate map transforms the equations of equilibrium and the kinematic conditions, thus giving rise to a new non-physical medium within which the waves decay. As discussed by Kausel [9,10], this artificial PML medium cannot be viewed as a standard viscoelastic medium, since the associated elasticity tensor lacks the minor symmetries.

Chew and Liu [11] were the first to derive a PML for elastic waves using a split-field approach. We note that the vast majority of the formulations, whether for electromagnetics, acoustics, or elastodynamics, were based on split-field formulations, where the displacement (or velocity) components were split into components that were propagating perpendicular to the truncation boundary and components that were tangential to it, thereby significantly increasing the number of unknowns and the computational cost. Basu and Chopra [12] were the first to formulate an unsplit-field PML, initially for time-harmonic problems [12], and later for transient elastodynamics [13–15]: however, the resulting semi-discrete forms include an internal force term, in addition to mass-, stiffness-, and damping-like matrices, requiring the storage of strains, as well as the temporal integration of the strains at every time step –a convoluted scheme that also destroyed the, originally, second-order in time character of the elastic waves.

To preserve the second-order character, Kucukcoban and Kallivokas [16,17] developed a symmetric formulation in 2D using a mixed-field approach for the PML, whereby both displacements and stresses were treated as unknowns, yet were approximated by standard Lagrange-family finite elements, without the need to resort to specialized mixed elements. Their approach led to the easy coupling of the PML with a conventional displacement-only formulation for the interior domain, which also allowed the use of the standard Newmark method for time integration. The mixed-field formulation was later extended to the 3D case [18]; more recently, it was augmented with the addition of Rayleigh damping, and its versatility was demonstrated with the development of user-defined elements for incorporation into commercial finite element software codes [19,20].

While the above developments advanced the goal of numerically simulating propagating elastic waves in unbounded heterogeneous domains, they were not entirely problem-free: a key difficulty is related to the long-time stability in time-domain simulations. Error growth has been observed, which sometimes has been attributed to

waves impinging at grazing incidence on the PML [21,22], other times to the interaction of evanescent waves with body waves in the PML [23], but is always associated with the use of the original stretching function. An early conjecture [24] attributed the error growth to the fact that the standard stretching function exhibits a singularity at zero frequency, but a definitive proof remains elusive. Nevertheless, the conjecture led to a modified stretching function that removed the singularity through a frequency shift, and gave rise to the complex-frequency-shifted CFS-PML [25,26]. The presence of the frequency shift in the stretching function alters the spectral properties of the PML (compared to the standard stretching function), and, more importantly, increases the temporal complexity when the formulation is inverted in the time-domain: to date, all CFS-PML implementations require the evaluation of convolutions. More recently, Matzen [27] discussed a displacement-based, unsplit-field, convolutional CFS-PML finite element formulation in 2D, which was later extended by Xie et al. [28] in 3D: whereas in both [27,28], the explicit computations of convolutions was avoided, an auxiliary differential equation approach had to be adopted to reduce the computational burden related to the convolutions. A similar approach has been recently pursued by Zhuang et al. [29] in the framework of a Nearly PML (N-PML) technique [30]. The N-PML technique differs from the PML technique by an inexact variable change in the definition of the stretched coordinates. As a result, the governing differential equation has the same form in the N-PML as in the regular medium. Theoretically, N-PMLs are not perfectly matched, since the inexact variable change is only correct if the stretching functions are spatially constant.

It should be noted that not all implementations or parameterizations of the CFS-PML are capable of eliminating the long-time instabilities: Meza-Fajardo and Papageorgiou [31] showed that both the standard PML and the CFS-PML suffer from long-time instability, albeit the CFS-PML can alleviate it by delaying its onset when compared to the standard PML. Based on numerical experiments, we conjecture that, in fact, careful parameterization of the PML can indeed delay the onset but not completely eliminate the instability, whereas, by contrast, careful parameterization of the CFS-PML can in fact eliminate the instability.

The objective of this paper is to extend the unsplit mixed-field formulation proposed by Kucukcoban and Kallivokas [16,17] to the CFS-PML: with stability, computational efficacy, and implementational ease in mind, we aim at a non-convolutional formulation that results in a second-order semi-discrete form, readily amenable to standard integration schemes, and, thus, easy to incorporate in existing codes. To this end, we show that through the introduction of auxiliary fields, local to the CFS-PML only, it is possible to retain the second-order temporal character of the original problem, avoiding convolutions. The result is a CFS-PML fully described by a triad of mass, damping, and element matrices, derivable by standard finite element approximations. We note that a detailed discussion of the aforementioned stability conjecture is beyond the scope of this article, but numerical experiments will attest to the conjecture.

The rest of the paper is organized as follows: in Section 2, we review the PML/CFS-PML fundamentals; in Section 3, we derive the strong form of the governing equations of the CFS-PML. In Section 4, we reduce the convolutional CFS-PML to second-order via the introduction of auxiliary fields, and derive the associated semi-discrete form, following suitable approximation choices. Results of numerical experiments are discussed in Section 5, and conclusions are drawn in Section 6.

2. The PML and the CFS-PML stretching functions

Consider, without loss of generality, the domain depicted in Fig. 1a, excerpted from a two-dimensional, originally unbounded, heterogeneous elastic domain. The unboundedness of the physical domain is interrupted at $s = s_0$ through the introduction of an artificial truncation boundary. A PML buffer of width L_{PML}, terminated at $s = s_t$, is attached to the truncation boundary at $s = s_0$, where s denotes the coordinate normal to the truncation boundary. The physical domain is henceforth limited to the interior domain ($s < s_0$). We denote with $\mathbf{n}_s$ the outward unit normal on the interior domain-PML interface at s_0, pointing away from the interior domain.

To endow the PML buffer with wave-dissipative properties, the Navier equations governing the wave motion in the interior domain are assumed to hold in the PML, albeit the physical coordinate s is mapped onto a frequency-dependent complex coordinate $\tilde{s}$ as per the map [11,32]:

$$s \mapsto \tilde{s} = s_0 + \int_{s_0}^{s} \lambda_s(s', \omega)\, ds', \tag{1}$$

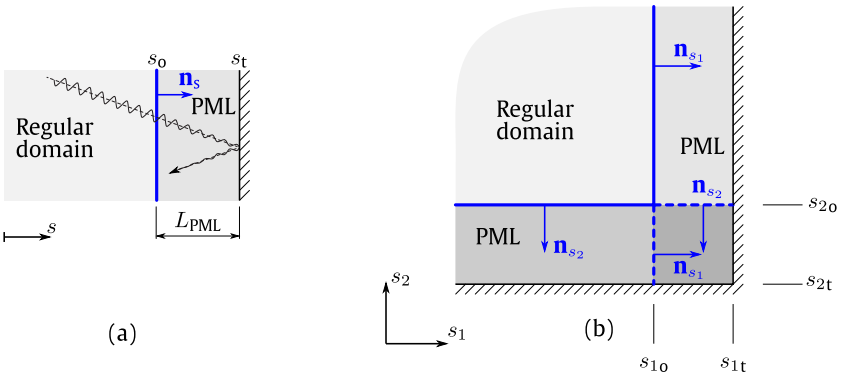

Fig. 1. Originally unbounded physical domain truncated through the introduction of a PML buffer: (a) PML concept; and (b) 2D PML buffer corner detail. The waves pass through the interface s_0 without reflections, and decay with distance within the PML.

where ω denotes circular frequency, and $\lambda_s(s,\omega)$ is the, so-called, stretching function. Differentiation of Eq. (1) yields:

$$\frac{d\tilde{s}}{ds} = \frac{d}{ds}\int_{s_0}^{s} \lambda_s(s',\omega)\, ds' = \lambda_s(s,\omega), \tag{2}$$

where it also holds that:

$$\frac{d}{d\tilde{s}} = \frac{1}{\lambda_s(s,\omega)}\frac{d}{ds}. \tag{3}$$

Various forms have been proposed for the stretching function λ_s. Of concern here are the standard (PML) and the complex-frequency-shifted (CFS-PML) stretching functions, defined as:

$$\lambda_s(s,\omega) = \begin{cases} \alpha_s(s) + \frac{\beta_s(s)}{i\omega} & \text{(PML)}, \\ \alpha_s(s) + \frac{\beta_s(s)}{\omega_s(s)+i\omega} & \text{(CFS-PML)}. \end{cases} \tag{4}$$

In the above, α_s is referred to as the scaling function that physically stretches the coordinate s, and, thereby, is responsible for the amplitude decay of the evanescent waves; β_s is referred to as the attenuation function that enforces amplitude decay of the propagating waves; and ω_s enforces a frequency shift that removes the frequency singularity at the origin for the second term of the stretching function, and, in principle, it too may depend on the spatial coordinate s. Clearly, when $\omega_s \equiv 0$, the CFS-PML stretching function reduces to the stretching function of the standard PML.

For the interface at s_0 to be reflectionless for all waves entering the PML, $\alpha_s(s_0,\omega) = 1$ and $\beta_s(s_0,\omega) = 0$. Consequently:

$$\lambda_s(s_0,\omega) = 1,\ \forall\,\omega. \tag{5}$$

Moreover, α_s and β_s should be positive, non-decreasing functions of s; common choices satisfying the above requirements include:

$$\alpha_s(s) = 1 + \alpha_0\left[\frac{(s-s_0)n_s}{L_{\text{PML}}}\right]^m, \tag{6}$$

$$\beta_s(s) = \beta_0\left[\frac{(s-s_0)n_s}{L_{\text{PML}}}\right]^m, \tag{7}$$

where α_0 and β_0 are parameters that control amplitude decay, and m denotes polynomial degree. Usually, β_0 should be chosen large enough to minimize the reflections from the fixed boundary of the PML buffer (at s_t). In practice, the choice of the scaling and attenuation functions is not straightforward and is closely related to the finite element discretization. For example, a large value of β_0 would require a finer mesh close to the interface at s_0 due to the rapid amplitude decay it imposes, but would, otherwise, allow for a coarser mesh close to the fixed boundary at s_t:

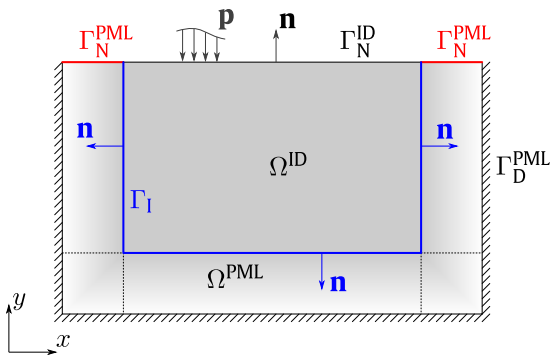

Fig. 2. PML-truncated semi-infinite domain Ω comprised of the regular elastic domain Ω^{ID} and the PML domain Ω^{PML}.

such requirements may be more onerous than the typical meshing guidelines associated with accuracy and numerical dispersion considerations in wave propagation problems.

While polynomial expressions similar to the ones used for the scaling and attenuation functions $\alpha_s(s)$ and $\beta_s(s)$ are also possible for the frequency shift function $\omega_s(s)$, the most common choice is a constant shift [21,24,33]. A spatially varying shift has been proposed by Roden and Gedney [34], and has been used in elastodynamics by Matzen [27] and Xie et al. [28] in the form of a decaying profile away from the interface s_0, as in:

$$\omega_s(s) = \omega_0 \left[\frac{(L_{\text{PML}} + s_0 - s) n_s}{L_{\text{PML}}} \right]^{m_2}, \tag{8}$$

where ω_0 is a parameter that controls the amplitude decay of $\omega_s(s)$, and m_2 is the polynomial degree ($m_2 = 1$ is a common choice).

We note that the complex coordinate stretching implied by the map (1) is uni-directional everywhere within the PML buffer, except at the corner subdomains (Fig. 1b), where the stretching extends along both $\mathbf{n}_{s1}$ and $\mathbf{n}_{s2}$.

3. The 2D unsplit-field CFS-PML for elastodynamics

Fig. 2 depicts a semi-infinite physical domain, truncated through the introduction of the PML buffer Ω^{PML}: the physical domain Ω^{ID} is now of finite extent, and henceforth referred to as the interior domain. The interface between the PML buffer and the interior domain is denoted by Γ_{I}; $\Gamma_{\text{N}}^{\text{ID}}$ denotes the interior domain's free surface, and $\Gamma_{\text{D}}^{\text{PML}}$ and $\Gamma_{\text{N}}^{\text{PML}}$ denote the Dirichlet and Neumann portions of the outer PML boundaries, respectively. We assume that Ω^{ID} is occupied by an elastic, arbitrarily heterogeneous material: we are interested in modeling the propagation of elastic waves in Ω^{ID}, including bulk and surface waves, when, for example, the free surface is subjected to prescribed time-dependent tractions. To address the time-domain formulation, we turn first to the dual frequency-domain problem.

3.1. Governing equations in the interior domain Ω^{ID}

The in-plane propagation of waves in the elastic domain Ω^{ID} is governed by the conservation of linear momentum (equilibrium), the kinematic conditions, and the constitutive relation. In the absence of body forces, the conservation of linear momentum reads[1]:

$$\mathbf{L}^{\text{T}} \hat{\boldsymbol{\sigma}} + \rho\, \omega^2\, \hat{\mathbf{u}} = \mathbf{0}, \tag{9}$$

where ρ denotes mass density. The vectors $\hat{\boldsymbol{\sigma}} = \left\{\hat{\sigma}_{xx}, \hat{\sigma}_{yy}, \hat{\sigma}_{xy}\right\}^{\text{T}}$, and $\hat{\mathbf{u}} = \left\{\hat{u}_x, \hat{u}_y\right\}^{\text{T}}$ collect stress and displacement components, respectively; a hat above a variable denotes the Fourier transform of the subtended quantity; and the

[1] Voigt notation, commonly used is standard finite element textbooks (e.g., [35–38]), is adopted in this paper.

functional dependence of $\hat{\boldsymbol{\sigma}}$ and $\hat{\mathbf{u}}$ on the spatial coordinates $\mathbf{x} = (x, y)$ and the frequency ω is implied, but has been dropped to reduce symbol congestion. The matrix $\mathbf{L}$ consists of differential operators, per:

$$\mathbf{L} = \begin{bmatrix} \frac{\partial}{\partial x} & 0 \\ 0 & \frac{\partial}{\partial y} \\ \frac{\partial}{\partial y} & \frac{\partial}{\partial x} \end{bmatrix}. \tag{10}$$

The strain vector $\hat{\boldsymbol{\epsilon}} = \left\{\hat{\epsilon}_{xx}, \hat{\epsilon}_{yy}, \hat{\gamma}_{xy}\right\}^{\mathrm{T}}$ is defined through the kinematic conditions[2]:

$$\hat{\boldsymbol{\epsilon}} = \mathbf{L}\hat{\mathbf{u}}, \tag{11}$$

and the constitutive relation for the linear elastic medium reads:

$$\hat{\boldsymbol{\sigma}} = \mathbf{C}\hat{\boldsymbol{\epsilon}}, \tag{12}$$

where $\mathbf{C}$ is the plane strain elasticity matrix, written in terms of the Lamé parameters λ and μ as:

$$\mathbf{C} = \begin{bmatrix} \lambda + 2\mu & \lambda & 0 \\ \lambda & \lambda + 2\mu & 0 \\ 0 & 0 & \mu \end{bmatrix}. \tag{13}$$

3.2. Governing equations in the PML buffer

In order to attenuate the waves in the PML buffer Ω^{PML}, the equilibrium equations (9) are transformed using the complex coordinate map (1): the transformation is applied to the partial derivatives of (10), by first setting $s = x$ in (1), and then $s = y$. There results:

$$\left(\frac{1}{\lambda_x}\mathbf{L}_x + \frac{1}{\lambda_y}\mathbf{L}_y\right)^{\mathrm{T}} \hat{\boldsymbol{\sigma}} + \rho\,\omega^2\,\hat{\mathbf{u}} = \mathbf{0}, \tag{14}$$

where the matrices of differential operators $\mathbf{L}_x$, $\mathbf{L}_y$ are defined as:

$$\mathbf{L}_x = \begin{bmatrix} \frac{\partial}{\partial x} & 0 \\ 0 & 0 \\ 0 & \frac{\partial}{\partial x} \end{bmatrix} \quad \text{and} \quad \mathbf{L}_y = \begin{bmatrix} 0 & 0 \\ 0 & \frac{\partial}{\partial y} \\ \frac{\partial}{\partial y} & 0 \end{bmatrix}. \tag{15}$$

Clearly, it holds that $\mathbf{L} = \mathbf{L}_x + \mathbf{L}_y$. Next, the transformed equilibrium equations (14) are multiplied by the product of the stretching functions $\lambda_x\lambda_y$ to yield:

$$\left(\lambda_y\,\mathbf{L}_x + \lambda_x\,\mathbf{L}_y\right)^{\mathrm{T}} \hat{\boldsymbol{\sigma}} + \rho\,\lambda_x\lambda_y\omega^2\,\hat{\mathbf{u}} = \mathbf{0}, \tag{16}$$

The kinematic conditions (11) are similarly transformed to yield:

$$\hat{\boldsymbol{\epsilon}} = \left(\frac{1}{\lambda_x}\mathbf{L}_x + \frac{1}{\lambda_y}\mathbf{L}_y\right)\hat{\mathbf{u}}. \tag{17}$$

As the constitutive law has no explicit spatial dependency, Eq. (12) holds also in the PML buffer Ω^{PML}. Thus, the set of the stretched equilibrium equations (16), the stretched kinematic conditions (17), and the constitutive relation (11) describe the dissipative governing equations for the PML.

3.3. Boundary and interface conditions

To complete the strong form of the boundary value problems for the interior domain Ω^{ID} and the PML buffer Ω^{PML}, the following boundary and interface conditions also hold; first, on the fixed exterior PML boundary:

$$\hat{\mathbf{u}} = \mathbf{0}, \quad \mathbf{x} \in \Gamma_{\mathrm{D}}^{\mathrm{PML}}, \tag{18}$$

[2] Here, γ_{xy} denotes the engineering shear strain.

while on the free surface $\Gamma_{\mathrm{N}}^{\mathrm{PML}}$ of the PML buffer we require that:

$$\lambda_x \lambda_y \hat{\mathbf{t}}^{(\mathbf{n})} = \mathbf{0}, \quad \mathbf{x} \in \Gamma_{\mathrm{N}}^{\mathrm{PML}}. \tag{19}$$

On the free surface of the interior domain $\Gamma_{\mathrm{N}}^{\mathrm{ID}}$, it holds:

$$\hat{\mathbf{t}}^{(\mathbf{n})} = 0, \quad \mathbf{x} \in \Gamma_{\mathrm{N}}^{\mathrm{ID}} \setminus \Gamma_{\mathrm{L}}^{\mathrm{ID}}, \quad \text{and} \quad \hat{\mathbf{t}}^{(\mathbf{n})} = \hat{\mathbf{p}}, \quad \mathbf{x} \in \Gamma_{\mathrm{L}}^{\mathrm{ID}}, \tag{20}$$

where $\hat{\mathbf{p}}$ denotes applied load on $\Gamma_{\mathrm{L}}^{\mathrm{ID}} \subset \Gamma_{\mathrm{N}}^{\mathrm{ID}}$, and $\hat{\mathbf{t}}^{(\mathbf{n})}$ is the traction vector defined, using customary notation, as:

$$\hat{\mathbf{t}}^{(\mathbf{n})} = \begin{bmatrix} \hat{\sigma}_{xx} n_x + \hat{\sigma}_{yx} n_y \\ \hat{\sigma}_{xy} n_x + \hat{\sigma}_{yy} n_y \end{bmatrix}. \tag{21}$$

Lastly, on the interface Γ_{I} between the interior domain and the PML buffer, continuity of displacements and of the tractions must hold:

$$\hat{\mathbf{u}}\big|_{\Gamma_{\mathrm{I}}^-} = \hat{\mathbf{u}}\big|_{\Gamma_{\mathrm{I}}^+}, \quad \text{and} \quad \hat{\mathbf{t}}^{(\mathbf{n})}\big|_{\Gamma_{\mathrm{I}}^-} = -\hat{\mathbf{t}}^{(\mathbf{n})}\big|_{\Gamma_{\mathrm{I}}^+} \tag{22}$$

where the notations Γ_{I}^- and Γ_{I}^+ denote limits as the interface Γ_{I} is approached from the interior domain, and the PML, respectively.

4. Multi-field finite element implementation

4.1. Weak forms

Following standard Galerkin weighted residual lines, the equilibrium equations (9) are first multiplied by kinematically admissible test functions $\hat{\mathbf{v}}$, and then integrated over the interior domain Ω^{ID}; after integration by parts and use of the divergence theorem, there results:

$$\int_{\Omega^{\mathrm{ID}}} \left(\mathbf{L}\hat{\mathbf{v}}\right)^{\mathrm{T}} \hat{\boldsymbol{\sigma}}\, dV - \omega^2 \int_{\Omega^{\mathrm{ID}}} \rho\, \hat{\mathbf{v}}^{\mathrm{T}} \hat{\mathbf{u}}\, dV = \int_{\Gamma_{\mathrm{I}}} \hat{\mathbf{v}}^{\mathrm{T}} \hat{\mathbf{t}}^{(\mathbf{n})}\, dA + \int_{\Gamma_{\mathrm{L}}^{\mathrm{ID}}} \hat{\mathbf{v}}^{\mathrm{T}} \hat{\mathbf{p}}\, dA. \tag{23}$$

Operating similarly on the equilibrium equations (16) of the PML buffer Ω^{PML}, and after taking into account the boundary conditions (18)–(19), we obtain:

$$\int_{\Omega^{\mathrm{PML}}} \left(\lambda_y \mathbf{L}_x \hat{\mathbf{v}} + \lambda_x \mathbf{L}_y \hat{\mathbf{v}}\right)^{\mathrm{T}} \hat{\boldsymbol{\sigma}}\, dV - \omega^2 \int_{\Omega^{\mathrm{PML}}} \rho\, \lambda_x \lambda_y\, \hat{\mathbf{v}}^{\mathrm{T}} \hat{\mathbf{u}}\, dV = -\int_{\Gamma_{\mathrm{I}}} \lambda_x \lambda_y \hat{\mathbf{v}}^{\mathrm{T}} \hat{\mathbf{t}}^{(\mathbf{n})}\, dA = -\int_{\Gamma_{\mathrm{I}}} \hat{\mathbf{v}}^{\mathrm{T}} \hat{\mathbf{t}}^{(\mathbf{n})}\, dA, \tag{24}$$

where the last equality is due to (5), which ensured that (by construction) $\lambda_x = \lambda_y = 1$ on Γ_{I}. Adding (23) and (24), while noting that the traction terms on Γ_{I} on the right-hand-side of (23) and (24) cancel out due to the continuity conditions (22), yields the sought weak form for the entire domain $\Omega^{\mathrm{ID}} \cup \Omega^{\mathrm{PML}}$:

$$\begin{aligned} &\int_{\Omega^{\mathrm{ID}}} \left(\mathbf{L}\hat{\mathbf{v}}\right)^{\mathrm{T}} \hat{\boldsymbol{\sigma}}\, dV - \omega^2 \int_{\Omega^{\mathrm{ID}}} \rho\, \hat{\mathbf{v}}^{\mathrm{T}} \hat{\mathbf{u}}\, dV + \int_{\Omega^{\mathrm{PML}}} \left(\lambda_y \mathbf{L}_x \hat{\mathbf{v}} + \lambda_x \mathbf{L}_y \hat{\mathbf{v}}\right)^{\mathrm{T}} \hat{\boldsymbol{\sigma}}\, dV - \omega^2 \int_{\Omega^{\mathrm{PML}}} \rho\, \lambda_x \lambda_y\, \hat{\mathbf{v}}^{\mathrm{T}} \hat{\mathbf{u}}\, dV \\ &\quad = \int_{\Gamma_{\mathrm{L}}^{\mathrm{ID}}} \hat{\mathbf{v}}^{\mathrm{T}} \hat{\mathbf{p}}\, dA. \end{aligned} \tag{25}$$

Upon substitution of the constitutive law (12) and the kinematic conditions (11) in (25), and the subsequent introduction of approximations for the trial $\hat{\mathbf{u}}$ and the test functions $\hat{\mathbf{v}}$, the first two terms of (25) will return the standard stiffness and consistent mass matrices of a displacement-based elastodynamics formulation for the interior domain. Of interest are the remaining two terms on the left-hand-side of (25), which are defined over the PML buffer only; to discuss their effect, we collect both terms in S^{PML}, defined as:

$$S^{\mathrm{PML}} = \int_{\Omega^{\mathrm{PML}}} \left(\lambda_y \mathbf{L}_x \hat{\mathbf{v}} + \lambda_x \mathbf{L}_y \hat{\mathbf{v}}\right)^{\mathrm{T}} \hat{\boldsymbol{\sigma}}\, dV - \omega^2 \int_{\Omega^{\mathrm{PML}}} \rho\, \lambda_x \lambda_y\, \hat{\mathbf{v}}^{\mathrm{T}} \hat{\mathbf{u}}\, dV. \tag{26}$$

Next, introduction of the constitutive law (12) and of the stretched kinematic conditions (17) in (26) yields:

$$S^{\mathrm{PML}} = \int_{\Omega^{\mathrm{PML}}} \left(\lambda_y \mathbf{L}_x \hat{\mathbf{v}} + \lambda_x \mathbf{L}_y \hat{\mathbf{v}}\right)^{\mathrm{T}} \mathbf{C} \left(\frac{1}{\lambda_x}\mathbf{L}_x + \frac{1}{\lambda_y}\mathbf{L}_y\right) \hat{\mathbf{u}}\, dV - \omega^2 \int_{\Omega^{\mathrm{PML}}} \rho\, \lambda_x \lambda_y\, \hat{\mathbf{v}}^{\mathrm{T}} \hat{\mathbf{u}}\, dV, \tag{27}$$

which can be rewritten as:

$$S^{\mathrm{PML}} = \int_{\Omega^{\mathrm{PML}}} \left[\frac{\lambda_y}{\lambda_x} \left(\mathbf{L}_x \hat{\mathbf{v}}\right)^{\mathrm{T}} \mathbf{C}\, \mathbf{L}_x + \frac{\lambda_x}{\lambda_y} \left(\mathbf{L}_y \hat{\mathbf{v}}\right)^{\mathrm{T}} \mathbf{C}\, \mathbf{L}_y + \left(\mathbf{L}_x \hat{\mathbf{v}}\right)^{\mathrm{T}} \mathbf{C}\, \mathbf{L}_y + \left(\mathbf{L}_y \hat{\mathbf{v}}\right)^{\mathrm{T}} \mathbf{C}\, \mathbf{L}_x \right] \hat{\mathbf{u}}\, dV - \omega^2 \int_{\Omega^{\mathrm{PML}}} \rho\, \lambda_x \lambda_y\, \hat{\mathbf{v}}^{\mathrm{T}} \hat{\mathbf{u}}\, dV. \tag{28}$$

As cast, (28), upon introduction of approximations for the trial function $\hat{\mathbf{u}}$ and the test function $\hat{\mathbf{v}}$, will contain displacement degrees-of-freedom within the PML buffer only. However, as discussed next, to remove the convolutions associated with time-domain implementations of (28), we introduce auxiliary fields that, though they add to the degrees-of-freedom within the PML, they also succeed in reducing the temporal complexity to advantage.

4.2. Multi-field CFS-PML decomposition

Eq. (28) describes fully the effect of the CFS-PML buffer. Due to the presence of the terms involving the stretching functions λ_x and λ_y, inverting S^{PML} in the time-domain would result in a convolutional form (see, for example, [28]). In order to bypass the undesirable numerical evaluations of convolutions and arrive at a second-order form, consistent with the interior domain's temporal order, we decompose the various terms implicated in the CFS-PML through the introduction of auxiliary variables, in a manner similar to the formulation of Kucukcoban and Kallivokas for the standard PML [16,17]. In the following, we introduce auxiliary strain-like and displacement-like variables: their introduction entails particular advantages, which will be discussed in detail once the discrete form is obtained.

To aid in subsequent algebraic operations, consider again the definitions of the stretching function λ_s, with $s \in \{x, y\}$, which we recast as:

$$\lambda_s(s,\omega) = \alpha_s + \frac{\beta_s}{\omega_s + i\omega} = \frac{\alpha_s\omega_s + \beta_s + i\omega\,\alpha_s}{\omega_s + i\omega} = \frac{A_s(s,\omega)}{B_s(s,\omega)}. \tag{29}$$

Therefore:

$$A_x = \alpha_x\omega_x + \beta_x + i\omega\alpha_x, \quad B_x = \omega_x + i\omega, \quad A_y = \alpha_y\omega_y + \beta_y + i\omega\alpha_y, \quad B_y = \omega_y + i\omega. \tag{30}$$

Moreover, the various cross-products of A_x, A_y, B_x and B_y are given as:

$$\begin{aligned} A_xA_y &= \underbrace{(\alpha_x\omega_x + \beta_x)\left(\alpha_y\omega_y + \beta_y\right)}_{a_0} + \underbrace{\left(\alpha_x\left(\alpha_y\omega_y + \beta_y\right) + \alpha_y\left(\alpha_x\omega_x + \beta_x\right)\right)}_{a_1}(i\omega) + \underbrace{\alpha_x\alpha_y}_{a_2}(i\omega)^2 \\ &= a_0 + a_1(i\omega) + a_2(i\omega)^2, \end{aligned} \tag{31}$$

$$\begin{aligned} B_xB_y &= \underbrace{\omega_x\omega_y}_{b_0} + \underbrace{\left(\omega_x + \omega_y\right)}_{b_1}(i\omega) + \underbrace{1}_{b_2}(i\omega)^2 \\ &= b_0 + b_1(i\omega) + b_2(i\omega)^2, \end{aligned} \tag{32}$$

$$\begin{aligned} A_xB_y &= \underbrace{(\alpha_x\omega_x + \beta_x)\,\omega_y}_{\gamma_0} + \underbrace{\left(\alpha_x\left(\omega_x + \omega_y\right) + \beta_x\right)}_{\gamma_1}(i\omega) + \underbrace{\alpha_x}_{\gamma_2}(i\omega)^2 \\ &= \gamma_0 + \gamma_1(i\omega) + \gamma_2(i\omega)^2, \end{aligned} \tag{33}$$

$$\begin{aligned} A_yB_x &= \underbrace{\left(\alpha_y\omega_y + \beta_y\right)\omega_x}_{\delta_0} + \underbrace{\left(\alpha_y\left(\omega_x + \omega_y\right) + \beta_y\right)}_{\delta_1}(i\omega) + \underbrace{\alpha_y}_{\delta_2}(i\omega)^2 \\ &= \delta_0 + \delta_1(i\omega) + \delta_2(i\omega)^2, \end{aligned} \tag{34}$$

where the parameters a_0, a_1, a_2, b_0, b_1, γ_0, γ_1, γ_2, δ_0, δ_1, and δ_2, depend on both x and y, due to the spatial variability of the stretching function components (α_x, β_x, ω_x and α_y, β_y, ω_y), but are otherwise independent of the frequency ω.

Next, we introduce auxiliary strain-like fields $\hat{\boldsymbol{\xi}}$ and $\hat{\boldsymbol{\eta}}$ by subtracting and adding like terms to $\lambda_y/\lambda_x \mathbf{L}_x\hat{\mathbf{u}}$ and $\lambda_x/\lambda_y \mathbf{L}_y\hat{\mathbf{u}}$, respectively:

$$\frac{\lambda_y}{\lambda_x}\mathbf{L}_x\hat{\mathbf{u}} = \mathbf{L}_\xi \underbrace{\left(\frac{\lambda_y}{\lambda_x} - \frac{\alpha_y}{\alpha_x}\right)\frac{\partial\hat{\mathbf{u}}}{\partial x}}_{\hat{\boldsymbol{\xi}}} + \frac{\alpha_y}{\alpha_x}\mathbf{L}_x\hat{\mathbf{u}}, \tag{35}$$

and similarly:

$$\frac{\lambda_x}{\lambda_y}\mathbf{L}_y\hat{\mathbf{u}} = \mathbf{L}_\eta \underbrace{\left(\frac{\lambda_x}{\lambda_y} - \frac{\alpha_x}{\alpha_y}\right)\frac{\partial\hat{\mathbf{u}}}{\partial y}}_{\hat{\boldsymbol{\eta}}} + \frac{\alpha_x}{\alpha_y}\mathbf{L}_y\hat{\mathbf{u}}, \tag{36}$$

where the strain-like fields $\hat{\boldsymbol{\xi}}$ and $\hat{\boldsymbol{\eta}}$ are defined as:

$$\hat{\boldsymbol{\xi}} = \left(\frac{\lambda_y}{\lambda_x} - \frac{\alpha_y}{\alpha_x}\right)\frac{\partial\hat{\mathbf{u}}}{\partial x}, \tag{37}$$

and

$$\hat{\boldsymbol{\eta}} = \left(\frac{\lambda_x}{\lambda_y} - \frac{\alpha_x}{\alpha_y}\right)\frac{\partial\hat{\mathbf{u}}}{\partial y}, \tag{38}$$

with

$$\mathbf{L}_\xi = \begin{bmatrix} 1 & 0 \\ 0 & 0 \\ 0 & 1 \end{bmatrix} \qquad \text{and} \qquad \mathbf{L}_\eta = \begin{bmatrix} 0 & 0 \\ 1 & 0 \\ 0 & 1 \end{bmatrix} \tag{39}$$

denoting selection matrices. We note that, while $\hat{\boldsymbol{\xi}}$ and $\hat{\boldsymbol{\eta}}$ contain derivatives of the displacement vector, and are therefore strain-like quantities, they possess only two components. Next, in addition to (37)–(38), we introduce an auxiliary displacement-like field $\hat{\mathbf{u}}$, defined as:

$$\hat{\mathbf{u}} = \left[\frac{(i\omega)^2}{B_x B_y} - 1\right]\hat{\mathbf{u}}. \tag{40}$$

The bracketed term in Eq. (40) can be interpreted as a filter, and, thus, $\hat{\mathbf{u}}$ can be seen as a filtered displacement. Eq. (40), with the aid of (30), allows us to rewrite the term $(i\omega)^2\,\lambda_x\lambda_y\,\hat{\mathbf{u}}$ that appears in Eq. (28) as:

$$(i\omega)^2\,\lambda_x\lambda_y\,\hat{\mathbf{u}} = A_x A_y\left(\hat{\mathbf{u}} + \hat{\mathbf{u}}\right). \tag{41}$$

Next, we introduce (41) and the auxiliary fields $\hat{\boldsymbol{\xi}}$, $\hat{\boldsymbol{\eta}}$, and $\hat{\mathbf{u}}$ into S^{PML} of (28), which becomes:

$$\begin{aligned} S^{\text{PML}} = &\int_{\Omega^{\text{PML}}} \left[\frac{\alpha_y}{\alpha_x}\left(\mathbf{L}_x\hat{\mathbf{v}}\right)^{\mathrm{T}}\mathbf{C}\mathbf{L}_x + \frac{\alpha_x}{\alpha_y}\left(\mathbf{L}_y\hat{\mathbf{v}}\right)^{\mathrm{T}}\mathbf{C}\mathbf{L}_y + \left(\mathbf{L}_x\hat{\mathbf{v}}\right)^{\mathrm{T}}\mathbf{C}\mathbf{L}_y + \left(\mathbf{L}_y\hat{\mathbf{v}}\right)^{\mathrm{T}}\mathbf{C}\mathbf{L}_x + \rho\,A_x A_y\,\hat{\mathbf{v}}^{\mathrm{T}}\right]\hat{\mathbf{u}}\,dV \\ &+ \int_{\Omega^{\text{PML}}} \left[\left(\mathbf{L}_x\hat{\mathbf{v}}\right)^{\mathrm{T}}\mathbf{C}\mathbf{L}_\xi\right]\hat{\boldsymbol{\xi}}\,dV + \int_{\Omega^{\text{PML}}} \left[\left(\mathbf{L}_y\hat{\mathbf{v}}\right)^{\mathrm{T}}\mathbf{C}\mathbf{L}_\eta\right]\hat{\boldsymbol{\eta}}\,dV + \int_{\Omega^{\text{PML}}} \rho\,A_x A_y\,\hat{\mathbf{v}}^{\mathrm{T}}\hat{\mathbf{u}}\,dV. \end{aligned} \tag{42}$$

Eq. (42), together with the weak imposition of definitions (37), (38), and (40) constitute the *multi-field* CFS-PML equivalent to the displacement-only CFS-PML of (28). To complete the equivalence, we conclude with the weak forms of (37), (38), and (40), using test functions $\hat{\mathbf{v}}_\xi$, $\hat{\mathbf{v}}_\eta$, and $\hat{\mathbf{v}}_{\text{u}}$, respectively:

$$\int_{\Omega^{\text{PML}}} A_x B_y \hat{\mathbf{v}}_\xi^{\mathrm{T}}\hat{\boldsymbol{\xi}}\,dV - \int_{\Omega^{\text{PML}}} \left(A_y B_x - \frac{\alpha_y}{\alpha_x}A_x B_y\right)\hat{\mathbf{v}}_\xi^{\mathrm{T}}\frac{\partial\hat{\mathbf{u}}}{\partial x}\,dV = 0, \tag{43}$$

$$\int_{\Omega^{\text{PML}}} A_y B_x \hat{\mathbf{v}}_\eta^{\mathrm{T}}\hat{\boldsymbol{\eta}}\,dV - \int_{\Omega^{\text{PML}}} \left(A_x B_y - \frac{\alpha_x}{\alpha_y}A_y B_x\right)\hat{\mathbf{v}}_\eta^{\mathrm{T}}\frac{\partial\hat{\mathbf{u}}}{\partial y}\,dV = 0, \tag{44}$$

$$\int_{\Omega^{\text{PML}}} B_x B_y \hat{\mathbf{v}}_{\text{u}}^{\mathrm{T}}\hat{\mathbf{u}}\,dV - \int_{\Omega^{\text{PML}}} \left[(i\omega)^2 - B_x B_y\right]\hat{\mathbf{v}}_{\text{u}}^{\mathrm{T}}\hat{\mathbf{u}}\,dV = 0. \tag{45}$$

4.3. The discrete form of the CFS-PML

Following a standard Galerkin procedure, we use the same standard approximants (e.g., Lagrange, spectral, serendipity, etc.) for both the trial and test functions implicated in the multi-field CFS-PML weak forms (42)–(45). Accordingly, let[3]:

$$\hat{\mathbf{u}}(\mathbf{x},\omega) \approx \mathbf{N}_{\mathrm{u}}(\mathbf{x})\hat{\mathbf{U}}, \quad \hat{\mathbf{v}}(\mathbf{x},\omega) \approx \mathbf{N}_{\mathrm{u}}(\mathbf{x})\hat{\mathbf{V}}, \tag{46}$$

$$\hat{\boldsymbol{\xi}}(\mathbf{x},\omega) \approx \mathbf{N}_{\xi}(\mathbf{x})\hat{\boldsymbol{\Xi}}, \quad \hat{\mathbf{v}}_{\xi}(\mathbf{x},\omega) \approx \mathbf{N}_{\xi}(\mathbf{x})\hat{\mathbf{V}}_{\xi}, \tag{47}$$

$$\hat{\boldsymbol{\eta}}(\mathbf{x},\omega) \approx \mathbf{N}_{\eta}(\mathbf{x})\hat{\mathbf{H}}, \quad \hat{\mathbf{v}}_{\eta}(\mathbf{x},\omega) \approx \mathbf{N}_{\eta}(\mathbf{x})\hat{\mathbf{V}}_{\eta}, \tag{48}$$

$$\hat{\mathbf{u}}(\mathbf{x},\omega) \approx \mathbf{N}_{\mathrm{u}}(\mathbf{x})\hat{\underline{\mathfrak{U}}}, \quad \hat{\mathbf{v}}_{\mathrm{u}}(\mathbf{x},\omega) \approx \mathbf{N}_{\mathrm{u}}(\mathbf{x})\hat{\mathbf{V}}_{\mathrm{u}}, \tag{49}$$

where $\mathbf{N}_{\mathrm{u}}(\mathbf{x})$, $\mathbf{N}_{\xi}(\mathbf{x})$, $\mathbf{N}_{\eta}(\mathbf{x})$, and $\mathbf{N}_{\mathrm{u}}(\mathbf{x})$ are (global) shape functions and $\hat{\mathbf{U}}$, $\hat{\boldsymbol{\Xi}}$, $\hat{\mathbf{H}}$, and $\hat{\mathfrak{U}}$ collect nodal displacements and auxiliary variables. Introducing (46)–(49) into (42)–(45) results in:

$$\begin{aligned} S^{\mathrm{PML}} = \mathbf{V}^T \left[\int_{\Omega^{\mathrm{PML}}} \left(\frac{\alpha_y}{\alpha_x} \mathbf{B}_x^{\mathrm{T}} \mathbf{C} \mathbf{B}_x + \frac{\alpha_x}{\alpha_y} \mathbf{B}_y^{\mathrm{T}} \mathbf{C} \mathbf{B}_y + \mathbf{B}_x^{\mathrm{T}} \mathbf{C} \mathbf{B}_y + \mathbf{B}_y^{\mathrm{T}} \mathbf{C} \mathbf{B}_x + \rho\, A_x A_y\, \mathbf{N}_{\mathrm{u}}^{\mathrm{T}} \mathbf{N}_{\mathrm{u}} \right) dV \right] \hat{\mathbf{U}}. \\ + \mathbf{V}_{\xi}^T \left[\int_{\Omega^{\mathrm{PML}}} \mathbf{B}_x^{\mathrm{T}} \mathbf{C} \mathbf{B}_{\xi}\, dV \right] \hat{\boldsymbol{\Xi}} + \mathbf{V}_{\eta}^T \left[\int_{\Omega^{\mathrm{PML}}} \mathbf{B}_y^{\mathrm{T}} \mathbf{C} \mathbf{B}_{\eta}\, dV \right] \hat{\mathbf{H}} + \mathbf{V}_{\mathrm{u}}^T \left[\int_{\Omega^{\mathrm{PML}}} \rho\, A_x A_y\, \mathbf{N}_{\mathrm{u}}^{\mathrm{T}} \mathbf{N}_{\mathrm{u}}\, dV \right] \hat{\mathfrak{U}}. \end{aligned} \tag{50}$$

$$\mathbf{V}_{\xi}^T \left[\int_{\Omega^{\mathrm{PML}}} A_x B_y \mathbf{N}_{\xi}^{\mathrm{T}} \mathbf{N}_{\xi}\, dV \right] \hat{\boldsymbol{\Xi}} - \mathbf{V}_{\xi}^T \left[\int_{\Omega^{\mathrm{PML}}} \left(A_y B_x - \frac{\alpha_y}{\alpha_x} A_x B_y \right) \mathbf{N}_{\xi}^{\mathrm{T}} \mathbf{L}_{\xi}^{\mathrm{T}} \mathbf{B}_x\, dV \right] \hat{\mathbf{U}} = 0. \tag{51}$$

$$\mathbf{V}_{\eta}^T \left[\int_{\Omega^{\mathrm{PML}}} A_y B_x \mathbf{N}_{\eta}^{\mathrm{T}} \mathbf{N}_{\eta}\, dV \right] \hat{\mathbf{H}} - \mathbf{V}_{\eta}^T \left[\int_{\Omega^{\mathrm{PML}}} \left(A_x B_y - \frac{\alpha_x}{\alpha_y} A_x B_y \right) \mathbf{N}_{\eta}^{\mathrm{T}} \mathbf{L}_{\eta}^{\mathrm{T}} \mathbf{B}_y\, dV \right] \hat{\mathbf{U}} = 0. \tag{52}$$

$$\mathbf{V}_{\mathrm{u}}^T \left[\int_{\Omega^{\mathrm{PML}}} B_x B_y \mathbf{N}_{\mathrm{u}}^{\mathrm{T}} \mathbf{N}_{\mathrm{u}}\, dV \right] \hat{\mathfrak{U}} - \mathbf{V}_{\mathrm{u}}^T \left[\int_{\Omega^{\mathrm{PML}}} \left((i\omega)^2 - B_x B_y \right) \mathbf{N}_{\mathrm{u}}^{\mathrm{T}} \mathbf{N}_{\mathrm{u}}\, dV \right] \hat{\mathbf{U}} = 0. \tag{53}$$

where $\mathbf{B}_x = \mathbf{L}_x \mathbf{N}_{\mathrm{u}}$, $\mathbf{B}_y = \mathbf{L}_y \mathbf{N}_{\mathrm{u}}$, $\mathbf{B}_{\xi} = \mathbf{L}_{\xi} \mathbf{N}_{\xi}$, and $\mathbf{B}_{\eta} = \mathbf{L}_{\eta} \mathbf{N}_{\eta}$. *Eqs.* (50)–(53) *are the discretized governing equations of the CFS-PML buffer zone*. We note that using the definitions (30)–(34) of the various coefficients implicated in the CFS-PML discrete form, the frequency ω in (50)–(53) appears to, at most, second power. Thus, reintroducing (50)–(53) into Eq. (25), yields the discrete form for the interior-domain-PML ensemble as:

$$\left(\mathbf{K} + i\omega \mathbf{C} - \omega^2 \mathbf{M} \right) \hat{\mathbf{d}} = \hat{\mathbf{f}}, \tag{54}$$

where the vector of nodal unknowns $\hat{\mathbf{d}}$ includes displacements, auxiliary strain fields, and the filtered displacements, i.e.:

$$\hat{\mathbf{d}} = \begin{Bmatrix} \hat{\mathbf{U}} \\ \hat{\boldsymbol{\Xi}} \\ \hat{\mathbf{H}} \\ \hat{\mathfrak{U}} \end{Bmatrix}. \tag{55}$$

We note again that the nodal displacement vector $\hat{\mathbf{U}}$ is defined over the entire domain $\Omega^{\mathrm{ID}} \cup \Omega^{\mathrm{PML}}$, whereas the nodal auxiliary vectors $\hat{\boldsymbol{\Xi}}$, $\hat{\mathbf{H}}$, and $\hat{\mathfrak{U}}$ are defined over the PML buffer only. The stiffness $\mathbf{K}$, damping $\mathbf{C}$, and mass matrices $\mathbf{M}$ are defined as:

$$\mathbf{K} = \mathbf{K}_{\mathrm{ID}} + \mathbf{K}_{\mathrm{PML}}, \quad \mathbf{C} = \mathbf{C}_{\mathrm{PML}}, \text{ and } \quad \mathbf{M} = \mathbf{M}_{\mathrm{ID}} + \mathbf{M}_{\mathrm{PML}}. \tag{56}$$

The contributions $\mathbf{K}_{\mathrm{ID}}$ and $\mathbf{M}_{\mathrm{ID}}$ to the global stiffness and mass matrices, respectively, are the standard stiffness and consistent mass matrices of a displacement-based finite element method for the interior domain Ω_{ID}, and are added to the global system matrices through a standard finite element assembly procedure. Similarly, the load vector $\hat{\mathbf{f}} = \left\{ \int_{\Gamma_{\mathrm{L}}^{\mathrm{ID}}} \mathbf{N}_{\mathrm{u}}^{\mathrm{T}} \hat{\mathbf{p}}\, dA, \mathbf{0}, \mathbf{0}, \mathbf{0} \right\}^{\mathrm{T}}$ corresponds to the loading vector along the boundary $\Gamma_{\mathrm{L}}^{\mathrm{ID}}$ of the interior domain. The

[3] While $\hat{\mathbf{u}}$ and $\hat{\mathbf{v}}$ are defined over $\Omega^{\mathrm{ID}} \cup \Omega^{\mathrm{PML}}$, the auxiliary fields $\hat{\boldsymbol{\xi}}$, $\hat{\boldsymbol{\eta}}$, $\hat{\mathbf{u}}$, and the corresponding test functions are defined over Ω^{PML} only.

stiffness matrix $\mathbf{K}_{\text{PML}}$ is defined as:

$$\mathbf{K}_{\text{PML}} = \int_{\Omega^{\text{PML}}} \begin{bmatrix} \frac{\alpha_y}{\alpha_x}\mathbf{B}_x^{\mathrm{T}}\mathbf{C}\mathbf{B}_x + \frac{\alpha_x}{\alpha_y}\mathbf{B}_y^{\mathrm{T}}\mathbf{C}\mathbf{B}_y + \mathbf{B}_x^{\mathrm{T}}\mathbf{C}\mathbf{B}_y & \mathbf{B}_x^{\mathrm{T}}\mathbf{C}\mathbf{B}_\xi & \mathbf{B}_y^{\mathrm{T}}\mathbf{C}\mathbf{B}_\eta & \rho a_0 \mathbf{N}_{\mathrm{u}}^{\mathrm{T}}\mathbf{N}_{\mathrm{u}} \\ +\mathbf{B}_y^{\mathrm{T}}\mathbf{C}\mathbf{B}_x + \rho a_0 \mathbf{N}_{\mathrm{u}}^{\mathrm{T}}\mathbf{N}_{\mathrm{u}} & & & \\ -\left(\delta_0 - \frac{\alpha_y}{\alpha_x}\gamma_0\right)\mathbf{N}_\xi^{\mathrm{T}}\mathbf{L}_\xi^{\mathrm{T}}\mathbf{B}_x & \gamma_0 \mathbf{N}_\xi^{\mathrm{T}}\mathbf{N}_\xi & \mathbf{0} & \mathbf{0} \\ -\left(\gamma_0 - \frac{\alpha_x}{\alpha_y}\delta_0\right)\mathbf{N}_\eta^{\mathrm{T}}\mathbf{L}_\eta^{\mathrm{T}}\mathbf{B}_y & \mathbf{0} & \delta_0 \mathbf{N}_\eta^{\mathrm{T}}\mathbf{N}_\eta & \mathbf{0} \\ b_0 \mathbf{N}_{\mathrm{u}}^{\mathrm{T}}\mathbf{N}_{\mathrm{u}} & \mathbf{0} & \mathbf{0} & b_0 \mathbf{N}_{\mathrm{u}}^{\mathrm{T}}\mathbf{N}_{\mathrm{u}} \end{bmatrix} dV. \tag{57}$$

Similarly, the damping matrix $\mathbf{C}_{\text{PML}}$ is:

$$\mathbf{C}_{\text{PML}} = \int_{\Omega^{\text{PML}}} \begin{bmatrix} \rho a_1 \mathbf{N}_{\mathrm{u}}^{\mathrm{T}}\mathbf{N}_{\mathrm{u}} & \mathbf{0} & \mathbf{0} & \rho a_1 \mathbf{N}_{\mathrm{u}}^{\mathrm{T}}\mathbf{N}_{\mathrm{u}} \\ -\left(\delta_1 - \frac{\alpha_y}{\alpha_x}\gamma_1\right)\mathbf{N}_\xi^{\mathrm{T}}\mathbf{L}_\xi^{\mathrm{T}}\mathbf{B}_x & \gamma_1 \mathbf{N}_\xi^{\mathrm{T}}\mathbf{N}_\xi & \mathbf{0} & \mathbf{0} \\ -\left(\gamma_1 - \frac{\alpha_x}{\alpha_y}\delta_1\right)\mathbf{N}_\eta^{\mathrm{T}}\mathbf{L}_\eta^{\mathrm{T}}\mathbf{B}_y & \mathbf{0} & \delta_1 \mathbf{N}_\eta^{\mathrm{T}}\mathbf{N}_\eta & \mathbf{0} \\ b_1 \mathbf{N}_{\mathrm{u}}^{\mathrm{T}}\mathbf{N}_{\mathrm{u}} & \mathbf{0} & \mathbf{0} & b_1 \mathbf{N}_{\mathrm{u}}^{\mathrm{T}}\mathbf{N}_{\mathrm{u}} \end{bmatrix} dV, \tag{58}$$

and the mass matrix $\mathbf{M}_{\text{PML}}$ is defined as:

$$\mathbf{M}_{\text{PML}} = \int_{\Omega^{\text{PML}}} \begin{bmatrix} \rho a_2 \mathbf{N}_{\mathrm{u}}^{\mathrm{T}}\mathbf{N}_{\mathrm{u}} & \mathbf{0} & \mathbf{0} & \rho a_2 \mathbf{N}_{\mathrm{u}}^{\mathrm{T}}\mathbf{N}_{\mathrm{u}} \\ -\left(\delta_2 - \frac{\alpha_y}{\alpha_x}\gamma_2\right)\mathbf{N}_\xi^{\mathrm{T}}\mathbf{L}_\xi^{\mathrm{T}}\mathbf{B}_x & \gamma_2 \mathbf{N}_\xi^{\mathrm{T}}\mathbf{N}_\xi & \mathbf{0} & \mathbf{0} \\ -\left(\gamma_2 - \frac{\alpha_x}{\alpha_y}\delta_2\right)\mathbf{N}_\eta^{\mathrm{T}}\mathbf{L}_\eta^{\mathrm{T}}\mathbf{B}_y & \mathbf{0} & \delta_2 \mathbf{N}_\eta^{\mathrm{T}}\mathbf{N}_\eta & \mathbf{0} \\ (b_2 - 1)\mathbf{N}_{\mathrm{u}}^{\mathrm{T}}\mathbf{N}_{\mathrm{u}} & \mathbf{0} & \mathbf{0} & b_2 \mathbf{N}_{\mathrm{u}}^{\mathrm{T}}\mathbf{N}_{\mathrm{u}} \end{bmatrix} dV. \tag{59}$$

In the above, the volume integrals over Ω^{PML} are evaluated using standard (full) Gaussian integration within the framework of isoparametric finite elements. Since the system matrices are frequency-independent, the frequency-domain system of equations (54) can be readily transformed back into the time-domain, resulting in:

$$(\mathbf{M}_{\text{ID}} + \mathbf{M}_{\text{PML}})\ddot{\mathbf{d}} + \mathbf{C}_{\text{PML}}\dot{\mathbf{d}} + (\mathbf{K}_{\text{ID}} + \mathbf{K}_{\text{PML}})\mathbf{d} = \mathbf{f}, \tag{60}$$

where a dot above a variable implies time differentiation. The resulting discretized system of equations (54) in the frequency-domain, or its counterpart (60) in the time-domain, recovered the familiar elastodynamics or structural dynamics form, and, thus the new formulation can be easily incorporated into existing finite element packages that allow for user-defined elements. Furthermore, Eq. (60) is non-convolutional and can be numerically integrated in time using standard implicit (e.g., Newmark's method) or explicit time integration schemes, readily available in most commercial software packages.

4.3.1. Relation to standard PML and to an elastic medium

Rewritten succinctly, the CFS-PML matrices admit the following structure:

$$\mathbf{K}_{\text{PML}} = \begin{bmatrix} \mathbf{K}_{\mathrm{uu}} & \mathbf{K}_{\mathrm{u}\xi} & \mathbf{K}_{\mathrm{u}\eta} & \mathbf{K}_{\mathrm{uu}} \\ \mathbf{K}_{\xi\mathrm{u}} & \mathbf{K}_{\xi\xi} & \mathbf{0} & \mathbf{0} \\ \mathbf{K}_{\eta\mathrm{u}} & \mathbf{0} & \mathbf{K}_{\eta\eta} & \mathbf{0} \\ \mathbf{K}_{\mathrm{uu}} & \mathbf{0} & \mathbf{0} & \mathbf{K}_{\mathrm{uu}} \end{bmatrix}, \quad \mathbf{C}_{\text{PML}} = \begin{bmatrix} \mathbf{C}_{\mathrm{uu}} & \mathbf{0} & \mathbf{0} & \mathbf{C}_{\mathrm{uu}} \\ \mathbf{C}_{\xi\mathrm{u}} & \mathbf{C}_{\xi\xi} & \mathbf{0} & \mathbf{0} \\ \mathbf{C}_{\eta\mathrm{u}} & \mathbf{0} & \mathbf{C}_{\eta\eta} & \mathbf{0} \\ \mathbf{C}_{\mathrm{uu}} & \mathbf{0} & \mathbf{0} & \mathbf{C}_{\mathrm{uu}} \end{bmatrix},$$

$$\text{and} \quad \mathbf{M}_{\text{PML}} = \begin{bmatrix} \mathbf{M}_{\mathrm{uu}} & \mathbf{0} & \mathbf{0} & \mathbf{M}_{\mathrm{uu}} \\ \mathbf{M}_{\xi\mathrm{u}} & \mathbf{M}_{\xi\xi} & \mathbf{0} & \mathbf{0} \\ \mathbf{M}_{\eta\mathrm{u}} & \mathbf{0} & \mathbf{M}_{\eta\eta} & \mathbf{0} \\ \mathbf{M}_{\mathrm{uu}} & \mathbf{0} & \mathbf{0} & \mathbf{M}_{\mathrm{uu}} \end{bmatrix}, \tag{61}$$

where the definitions of the individual submatrices can be directly inferred from (57)–(59). We note that, in the case of a standard PML, for which it holds that $\omega_x = \omega_y = 0$, the filtered displacement (40) vanishes identically,

and the parameters a_0, a_1, a_2, b_0, b_1, γ_0, γ_1, γ_2, δ_0, δ_1, and δ_2 reduce to:

$$\begin{array}{lll} a_0 = \beta_x\beta_y, & a_1 = \alpha_x\beta_y + \alpha_y\beta_x, & a_2 = \alpha_x\alpha_y, \\ b_0 = 0, & b_1 = 0, & b_2 = 1, \\ \gamma_0 = 0, & \gamma_1 = \beta_x, & \gamma_2 = \alpha_x, \\ \delta_0 = 0, & \delta_1 = \beta_y, & \delta_2 = \alpha_y. \end{array} \tag{62}$$

This leads to the following matrix structure, valid for the standard PML:

$$\mathbf{K}_{\text{PML}} = \begin{bmatrix} \mathbf{K}_{\text{uu}} & \mathbf{K}_{\text{u}\xi} & \mathbf{K}_{\text{u}\eta} \\ \mathbf{0} & \mathbf{0} & \mathbf{0} \\ \mathbf{0} & \mathbf{0} & \mathbf{0} \end{bmatrix}, \quad \mathbf{C}_{\text{PML}} = \begin{bmatrix} \mathbf{C}_{\text{uu}} & \mathbf{0} & \mathbf{0} \\ \mathbf{C}_{\xi\text{u}} & \mathbf{C}_{\xi\xi} & \mathbf{0} \\ \mathbf{C}_{\eta\text{u}} & \mathbf{0} & \mathbf{C}_{\eta\eta} \end{bmatrix}, \quad \mathbf{M}_{\text{PML}} = \begin{bmatrix} \mathbf{M}_{\text{uu}} & \mathbf{0} & \mathbf{0} \\ \mathbf{0} & \mathbf{M}_{\xi\xi} & \mathbf{0} \\ \mathbf{0} & \mathbf{0} & \mathbf{M}_{\eta\eta} \end{bmatrix}. \tag{63}$$

The matrices in Eq. (63) give rise to a new element for the standard PML, which entails advantages over the earlier (standard) PML elements derived in [16,17]. To compare, we first note that the matrices of the new PML element are non-symmetric and indefinite, whereas in [17] two PML elements were proposed, one defined by symmetric, yet indefinite, matrices, and a second characterized by non-symmetric, yet positive-definite, matrices. Moreover, the elements in [17] required 3 auxiliary fields (stress components), whereas herein we use 4 auxiliary fields ($\boldsymbol{\xi}$ and $\boldsymbol{\eta}$, with 2 components each). Thus, at first glance it appears that the earlier developed elements may have a computational advantage: however, the elements in [17] require same-order approximants for both the displacements and the stresses, whereas, as will be discussed in the next section, reduced-order approximants are possible for the auxiliary fields used herein, thus realizing a modest improvement on the computational cost over the earlier PML elements. It is noted that the overarching advantage of the present formulation is that the desired second-order character is enjoyed not only by the standard PML, but also has now been extended to the CFS-PML.

We note that in the case of a regular elastic medium, for which $\alpha_x = \alpha_y = 1$, $\beta_x = \beta_y = 0$, $\omega_x = \omega_y = 0$, the parameters a_0, a_1, a_2, b_0, b_1, γ_0, γ_1, γ_2, δ_0, δ_1, and δ_2 take the following values:

$$\begin{array}{lll} a_0 = 0, & a_1 = 0, & a_2 = 1, \\ b_0 = 0, & b_1 = 0, & b_2 = 1, \\ \gamma_0 = 0, & \gamma_1 = 0, & \gamma_2 = 1, \\ \delta_0 = 0, & \delta_1 = 0, & \delta_2 = 1. \end{array} \tag{64}$$

Accordingly, all auxiliary variables vanish identically, and the PML matrices (57)–(59) reduce to:

$$\mathbf{K}_{\text{PML}} = \mathbf{K}_{\text{uu}}, \quad \mathbf{C}_{\text{PML}} = \mathbf{0}, \quad \text{and} \quad \mathbf{M}_{\text{PML}} = \mathbf{M}_{\text{uu}}, \tag{65}$$

whose structure is identical to the interior problem's matrices.

4.4. CFS-PML element technology

Given the mixed-field implementation of the CFS-PML, it is of interest to minimize the number of additional degrees-of-freedom (DOF) introduced by the auxiliary fields. To this end, we explore the use of approximants $\mathbf{N}_\xi$, $\mathbf{N}_\eta$, and $\mathbf{N}_{\text{u}}$ for the auxiliary fields (Eqs. (47)–(49)) of order lower than the order of the approximants $\mathbf{N}_{\text{u}}$ used for the displacements (Eq. (46)). As is typically the case, of concern is that the choices of the particular approximant orders do not introduce spurious zero-energy modes [39], due to rank deficiency of the element stiffness matrix. Typically, this rank deficiency would result in spurious hourglass-shaped deformations, which in transient simulations would lead to instability. If realized, these zero-energy modes would require specialized stabilization schemes in order to avoid hourglassing, as first established by Belytschko et al. [40,41].

To address the concern, we turn to the structure of the system matrices (61), and note that the stiffness submatrix $\mathbf{K}_{\text{uu}}$ has full rank, and, therefore the displacement solution will always remain free of spurious zero-energy modes, irrespective of the order of the approximants for the auxiliary fields: the benefit lent by $\mathbf{K}_{\text{uu}}$ can be traced to the mixed-field formulation and the particular choices for the auxiliary fields (Eqs. (35) and (36)). It is important to note that the use of reduced-order approximants for the stresses in our earlier mixed-field displacement–stress formulation [16,17] would have triggered spurious zero-energy modes, resulting in hourglass instabilities in the computed response: therein lies an additional modest computational advantage the present mixed-field formulation has over the earlier one.

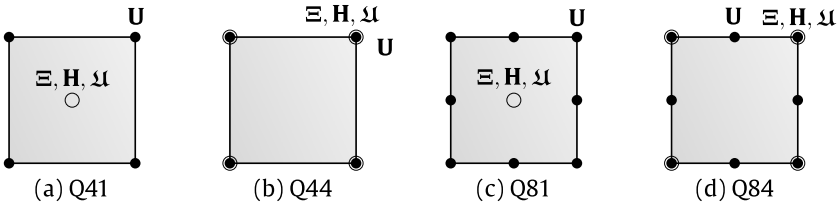

Fig. 3. Discretization of the displacement and auxiliary fields: (a) the Q41 element with a linear variation of $\hat{\mathbf{u}}$ and a constant $\hat{\boldsymbol{\xi}}$, $\hat{\boldsymbol{\eta}}$, and $\hat{\mathbf{u}}$; (b) the Q44 element with a bilinear variation of all variables; (c) the Q81 serendipity element with a quadratic variation of $\hat{\mathbf{u}}$ and a constant $\hat{\boldsymbol{\xi}}$, $\hat{\boldsymbol{\eta}}$, and $\hat{\mathbf{u}}$; and (d) the Q84 serendipity element with a quadratic variation of $\hat{\mathbf{u}}$ and a bilinear variation of $\hat{\boldsymbol{\xi}}$, $\hat{\boldsymbol{\eta}}$, and $\hat{\mathbf{u}}$.

Table 1
Degrees-of-freedom for various multi-field CFS-PML elements; the degrees-of-freedom for a standard single-field Q4 and Q8 element are indicated in gray.

Element	Number of DOF					
Type	**U**	**Ξ**	**H**	**𝔘**	Total	Average per element
Standard Q4	8	-	-	-	**8**	2
Multi-field Q41	8	2	2	2	**14**	8
Multi-field Q44	8	8	8	8	**32**	20
Standard Q8	16	-	-	-	**16**	6
Multi-field Q81	16	2	2	2	**22**	12
Multi-field Q84	16	8	8	8	**40**	28

With the above thoughts in mind, we consider next four different CFS-PML element types (Fig. 3). The first element type, henceforth referred to as the Q41 element, combines standard bilinear 4-noded shape functions (Q4) for the displacement field (shown with solid circles in Fig. 3) with a constant shape function for each of the auxiliary variables (shown with open circles in Fig. 3). A second CFS-PML element type – the Q44 element – employs bilinear shape functions for the displacements and the auxiliary variables. Similarly, CFS-PML elements Q81 and Q84 use 8-noded serendipity shape functions for the displacement field with a constant or bilinear approximations for the auxiliary variables, respectively.

The number of DOF for each of the CFS-PML multi-field elements is listed in Table 1 and is compared to the standard single-field Q4 and Q8 elements. As it can be seen, the Q41 and Q81 elements result in a modest increase of the number of DOF with respect to the Q4 and Q8 elements, respectively, whereas the number of DOF for the Q44 and Q84 elements is notably larger. Shown in Table 1 is also the average number of DOF per element in a, theoretically, infinite 2D mesh of rectangular elements: it appears that the Q81 element is particularly attractive, since it only doubles the number of DOF per element with respect to the standard Q8 element. We note that the construction of triangular CFS-PML elements follows lines similar to those pursued for the development of the quadrilateral elements.

5. Numerical examples

In this section, we demonstrate the use of the new CFS-PML elements with three case studies: a homogeneous halfspace, a waveguide, and a three-layered medium overlain a halfspace. The performance of the various CFS-PML element types of Section 4.4 is discussed, while results for both the standard PML and the CFS-PML are presented and compared.

5.1. Case 1: homogeneous halfspace

In the first case study, we model the response of a homogeneous solid occupying a halfspace, under plane strain conditions, when subjected to a vertical line load on the surface at the origin (Fig. 4). The solid has shear wave

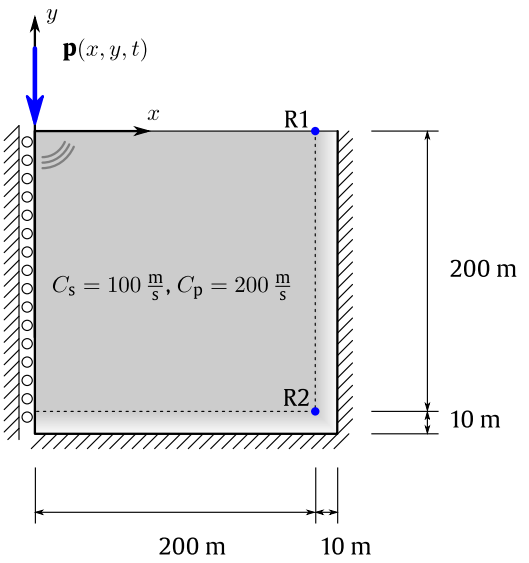

Fig. 4. PML-truncated semi-infinite domain.

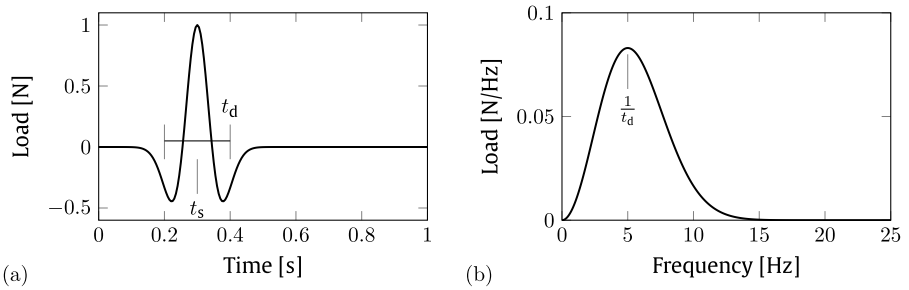

Fig. 5. (a) Time history; and (b) frequency content of a Ricker pulse with a characteristic period $t_d = 0.2$ s and time shift $t_s = 0.3$ s.

velocity $C_s = 100\ \frac{m}{s}$, dilatational wave speed $C_p = 200\ \frac{m}{s}$ (Poisson ratio $\nu = \frac{1}{3}$), and mass density $\rho = 1800\ \frac{kg}{m^3}$. The computational domain consists of an interior domain with a size of 200 m × 200 m, surrounded by a 10 m-thick PML buffer at the bottom and left side ($L_{PML} = 10$ m). The PML buffer is fixed along its outer edges, except along the free surface, while symmetry conditions are applied along the $x = 0$ edge. The line load $\mathbf{p}(x, y, t)$ is driven by a Ricker wavelet of unit amplitude, defined as:

$$\mathbf{p}(x, y, t) = \left(0, -\delta(x-0, y-0)\left[1 - 2\left(\frac{\pi(t-t_s)}{2-t_d}\right)^2\right]\exp\left[-\left(\frac{\pi(t-t_s)}{t_d}\right)^2\right]\right), \tag{66}$$

where $t_d = 0.2$ s is the characteristic period, and $t_s = 0.3$ s is the time shift. Fig. 5 depicts the time history and frequency content of the Ricker pulse, which has a dominant frequency of $1/t_d = 5$ Hz, and a spectral bandwidth of about 15 Hz.

To define the PML, we use a quadratic function for both β_x, and β_y ($m = 2$ in Eq. (7)), and set $\beta_0 = 20\, C_s/L_{PML}$. Conversely, α_0 is set to 0 (no physical stretching of the coordinates). Both the standard PML and the CFS-PML stretching function are considered: to obtain the standard PML, we set $\omega_x = \omega_y = 0$, and for the CFS-PML we set $\omega_x = \omega_y = \omega_0 = 5\pi$ rad/s. We note that, even though the formulation allows for spatially variable frequency shifts, herein we restrict the computational experiments to the use of a constant frequency shift ω_0 ($m_2 = 0$ in Eq. (8)); the selected value corresponds to the cut-off frequency of an elastic layer with a thickness equal to the PML's width $L_{PML} = 10$ m and a shear wave velocity $C_s = 100\ \frac{m}{s}$ ($\omega_0 = \frac{\pi}{2}\frac{C_s}{L_{PML}}$).

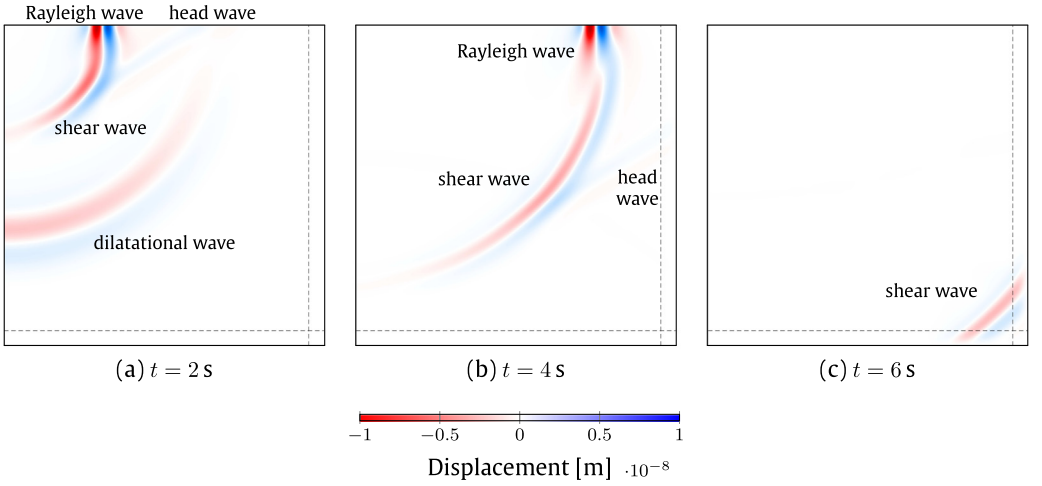

Fig. 6. Vertical displacement in the semi-infinite domain at (a) $t = 2$ s, (b) $t = 4$ s, and (c) $t = 6$ s for the Q81 element and CFS-PML shape function.

A mesh of 210 × 210 square elements of edge size equal to 1 m is used to discretize the computational domain. Standard displacement-based Q4 or Q8 finite elements are employed in the interior domain; the Q4 elements are enhanced with incompatible bending shape functions to preclude shear locking [42,43]. When the interior domain is meshed with the Q4 elements, then the PML buffer is meshed with either the Q41 or Q44 CFS-PML elements, and similarly, Q8 interior domain elements are coupled with Q81 or Q84 CFS-PML elements. The Newmark-β method is used for integrating the equations of motion in time, with the Newmark parameters set to $\beta = \frac{1}{4}$ and $\gamma = \frac{1}{2}$ (constant average acceleration) — a scheme that is energy conserving. A time step $\Delta t = 0.01$ s is used to compute the response for all element types and for both the standard PML and the CFS-PML stretching functions.

Fig. 6 shows the amplitude of the vertical displacement component at various time instances when the CFS-PML Q81 element is used[4]: at $t = 2$ s, the P-wave front, the S-wave front, the head wave, and the Rayleigh wave are clearly seen; at $t = 4$ s, the P-wave front has already been attenuated by the CFS-PML, as has a portion of the head wave; at $t = 6$ s the Rayleigh wave have been absorbed, while the tail end of the S-wave front is about to exit the computational domain. Thus, all waves are efficiently absorbed by the PML buffer with no discernible reflections; in addition, no spurious growth is observed. To complement the pictorial depiction of the reflectionless wave absorption, Fig. 7 shows the time histories of the horizontal and vertical displacement components at receivers R1 and R2 (Fig. 4), for all element types (Q81, Q84, Q41, and Q44): the Q41 and Q44 responses are virtually indistinguishable, as are the Q81 and Q84 traces. However, small differences exist between the different-order elements (e.g., Q81 versus Q41) due to numerical dispersion — typical of wave simulations where no special dispersion treatment has been implemented.

In order to further quantify the performance of the CFS-PML, we consider next an enlarged domain Ω^{ED} of size 410 m × 410 m with fixed exterior boundaries. The extended domain is discretized with the displacement-based Q4 and Q8 elements, respectively, and the response is recorded up to times that are prior to the arrival of any waves to Ω^{RD} from the part of the domain that is exterior to Ω^{RD}. The results $\mathbf{u}^{\mathrm{ED}}$ of the extended domain computation are compared against those obtained from the CFS-PML-truncated domain. In particular, in Fig. 8 we consider the normalized error histories $\left\| u_i - u_i^{\mathrm{ED}} \right\| / \max \left\| u_i^{\mathrm{ED}} \right\|$ of the displacement components at the receiver locations R1 and R2. As it can be seen therein, the error is approximately 3–7 orders smaller than the displacement amplitude, for all element types, and it can be further controlled by increasing the amplitude decay in the PML parameter through the value of the parameter β_0. As discussed by Kucukcoban and Kallivokas [17], this should be accompanied by a mesh refinement of the PML buffer to reduce numerical reflections.

To better quantify the PML's wave-absorptive behavior and its long-time behavior, we compute next the energy in the interior domain. Fig. 9 depicts the energy as a function of time for the four element types Q41, Q44, Q81,

[4] The results, using elements Q41, Q44, and Q84, are, visually, identical.

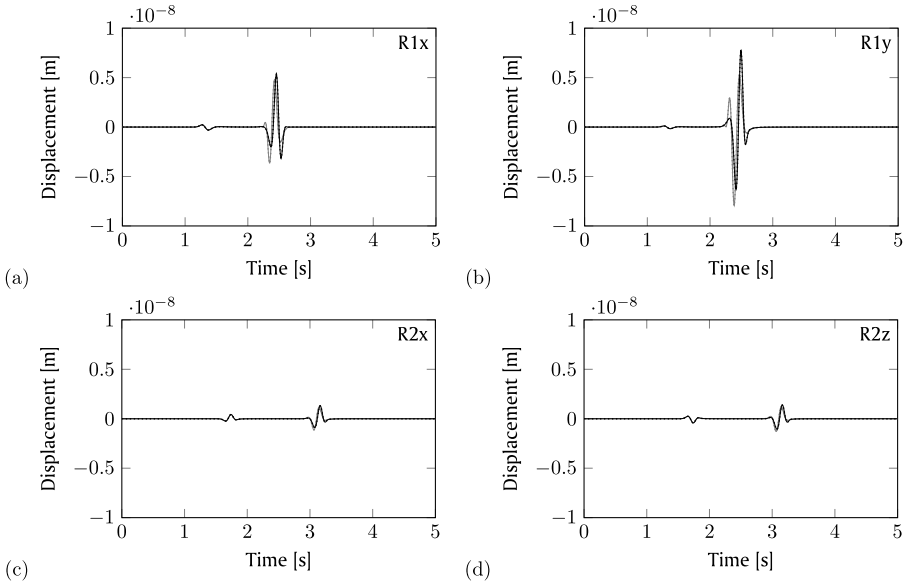

Fig. 7. Time history of the horizontal (left) and vertical (right) displacement components at receivers R1 (top) and R2 (bottom). The results are shown for the Q41 (solid gray), Q44 (dotted gray), Q81 (solid black), and Q84 (dotted black) elements.

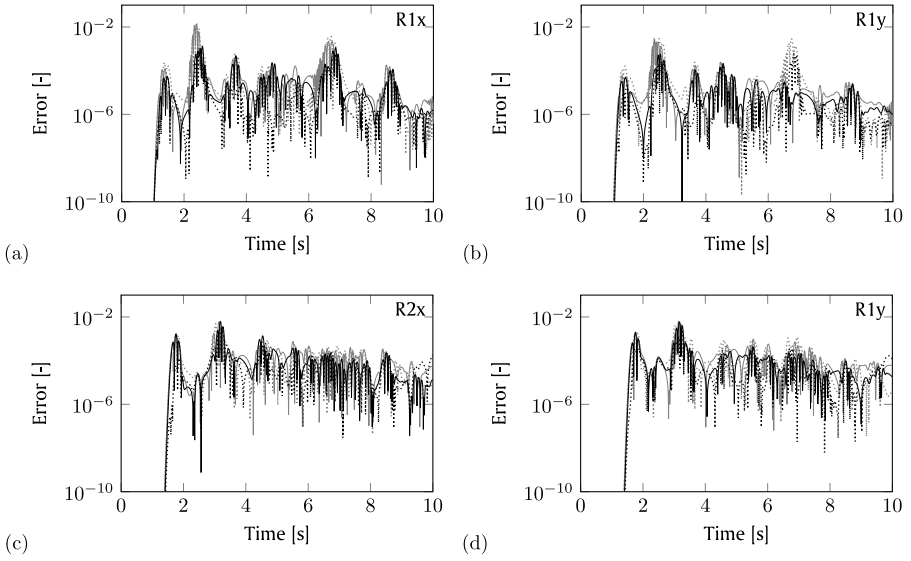

Fig. 8. Time history of the normalized error $\left\|u_i - u_i^{\mathrm{ED}}\right\| / \max \left\|u_i^{\mathrm{ED}}\right\|$ of the horizontal (left) and vertical (right) displacements at receivers R1 (top row), and R2 (bottom row). The results are shown for the Q41 (solid gray), Q44 (dotted gray), Q81 (solid black), and Q84 (dotted black) elements.

and Q88, and for both the standard PML (left column) and the CFS-PML (right column). The top figure row shows the energy using a linear scale between 0 s and 10 s, while the plots of the second figure row have been drawn in logarithmic scale for a much longer observation period (200 s). From the top figure row, the responses, using either the standard PML or the CFS-PML, appear identical. Specifically, it can be seen that after the pulse has entered its silent state at about $t = 0.5$ s, the energy plateaus until the P-wave exits the interior domain propagating into the PML buffer ($1\text{ s} < t < 2\text{ s}$); the energy then drops to a second plateau, which is subsequently maintained until the Rayleigh and S-waves reach the PML buffer and get themselves absorbed, starting at about $t = 3$ s.

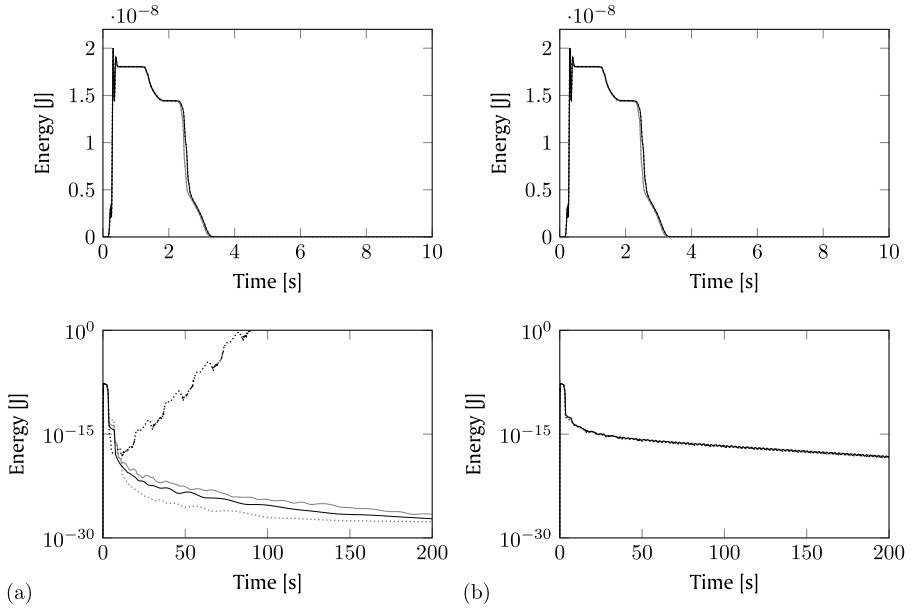

Fig. 9. Energy in the interior domain (case 1) for: (a) standard PML ($\omega_0 = 0$); and (b) CFS-PML ($\omega_0 = 5\,\text{rad/s}$). Results are shown for the Q41 (solid gray), Q44 (dotted gray), Q81 (solid black), and Q84 (solid black) elements. The results are plotted on a linear scale for $0 \le t \le 10$ s (top row), and on a logarithmic scale for $0 \le t \le 200$ s (second row).

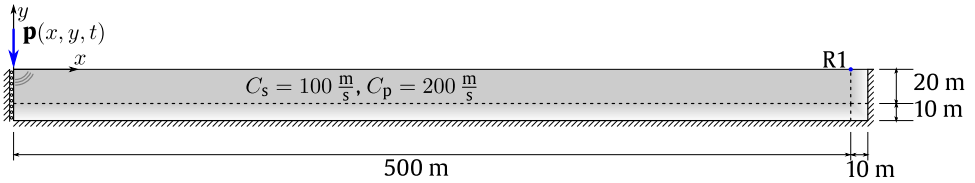

Fig. 10. PML-truncated semi-infinite shallow domain occupied by a homogeneous elastic solid.

While the responses obtained using the standard PML and the CFS-PML match well at early times, long-time instabilities arise for the standard PML: for example, using the Q84 PML element, spurious growth of the energy is observed from about $t = 10$ s (Fig. 9). By contrast, in this experiment, the Q41, Q44, and Q81 standard PML elements do not suffer from instabilities, but may be unstable for other domain geometries and loading, as will be shown in the next example. We note that the long-time instability of the standard PML has been reported elsewhere [21,22], though its origins, to date, have not been adequately traced or articulated. By contrast, the CFS-PML mitigates the spurious growth, resulting in a long-time energy decay for all element types.

5.2. Case 2: Homogeneous waveguide

In order to further study the spurious energy growth in the PML, we consider next the response of a shallow and long homogeneous domain (Fig. 10), bearing the same physical properties and loading as those of the preceding section's case. The interior domain is 500 m long and 20 m deep, and is surrounded by a 10 m-thick PML: the geometry is similar to one described by Festa and Vilotte in [21], and it is particularly prone to instabilities when evanescent (e.g. Rayleigh) waves enter the PML buffer at near-grazing angles. Thus, the numerical experiment of this section has been designed to trigger the reported instability, by setting the domain's depth to be approximately equal to the dominant Rayleigh wavelength (corresponding to the Ricker pulse's central frequency), thereby allowing lower-frequency Rayleigh waves to penetrate the PML buffer. The interior domain is meshed using 510×30 square elements with 1 m sides. The displacement-based Q4 or Q8 finite elements are employed in the interior domain,

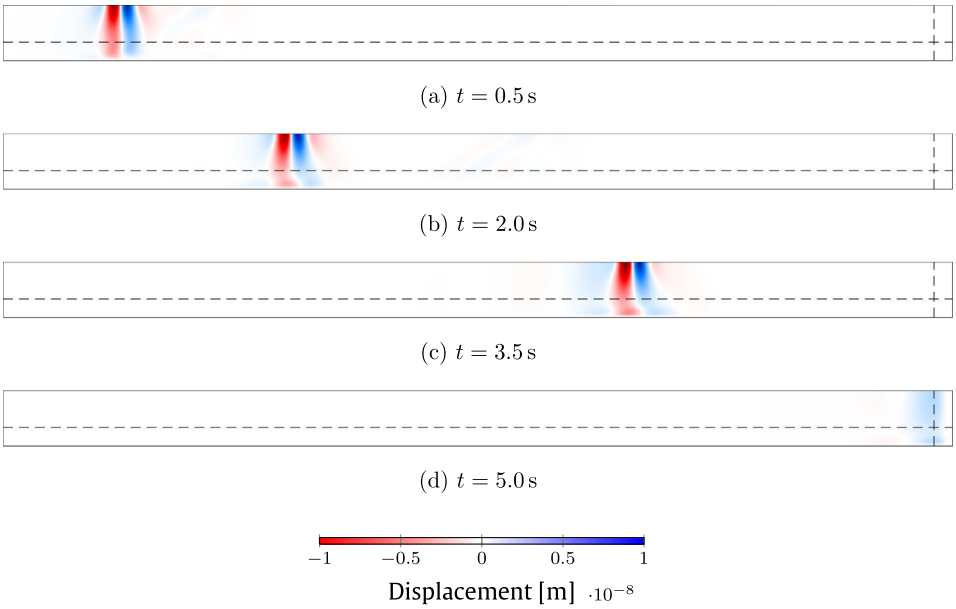

Fig. 11. Wavefield snapshots in a shallow elastic domain terminated by a standard PML buffer ($\omega_0 = 0$): (a) $t = 0.5$ s, (b) $t = 2.0$ s, (c) $t = 3.5$ s, and (d) $t = 5.0$ s.

whereas Q41, Q44, Q81, or Q84 elements are used for the PML buffer, and, similarly to the preceding case, the Newmark-β method is used with $\beta = \frac{1}{4}$ and $\gamma = \frac{1}{2}$ for marching in time.

Figs. 11 and 12 show snapshots of the response when the standard PML and the CFS-PML are used, respectively. The corresponding energy plots are shown in Fig. 15. We note that in the standard PML case (Fig. 11), the Rayleigh waves that penetrate the PML show amplitude growth as the waves travel to the right: the amplitude growth is particularly apparent near the fixed boundary of the PML, and, in turn, results in energy growth in the interior domain. This can also be seen in the time history at receiver R1 depicted in Fig. 13, where the amplitude growth results in spurious oscillations at about $t = 6$ s. By contrast, the use of the CFS-PML mitigates the spurious oscillations, as it can be seen in the time history depicted in Fig. 14.

As it can be seen in Fig. 15 (top left), the energy increases from $t = 1$ s to $t = 6$ s, prior to the waves exiting into the side PML buffer, and the energy no longer exhibits the plateau described in the preceding section. By contrast, the wavefield snapshots depicted in Fig. 12, which were obtained using the CFS-PML, do not exhibit growth: in particular, the motion amplitudes as the fixed PML boundary is approached have clearly decayed. Moreover, the energy has now plateaued, as shown in Fig. 15 (top right).

When the motion is recorded over long times, the exponential energy growth associated with the standard PML becomes plainly obvious, as shown in Fig. 15 (bottom left): the Q41, Q81, and Q84, endowed with the standard PML stretching function, exhibit error growth. The standard PML Q44 element also results in spurious energy growth, but, in the Q44 case, the PML corner is more effective than in the Q41, Q81, and Q84 cases in limiting the growth.

By contrast, all four of the new CFS-PML elements do not cause energy growth, resulting in stable long-time behavior, as it can be seen in Fig. 12 (bottom right). In addition, and similarly to the preceding section's case, the results for the Q41 and Q44 elements, and the Q81 and Q84 elements, respectively, are virtually indistinguishable, indicating that the additional DOF of the Q44 and Q84 elements contribute little to the absorptive capabilities of the elements.

5.3. Case 3: Layered medium

We consider next the response of a layered elastic medium, comprising two layers of 40 m and 80 m thickness, respectively, overlain on a homogeneous halfspace, as shown in Fig. 16. The shear wave velocity is $C_s = 100\,\frac{\mathrm{m}}{\mathrm{s}}$

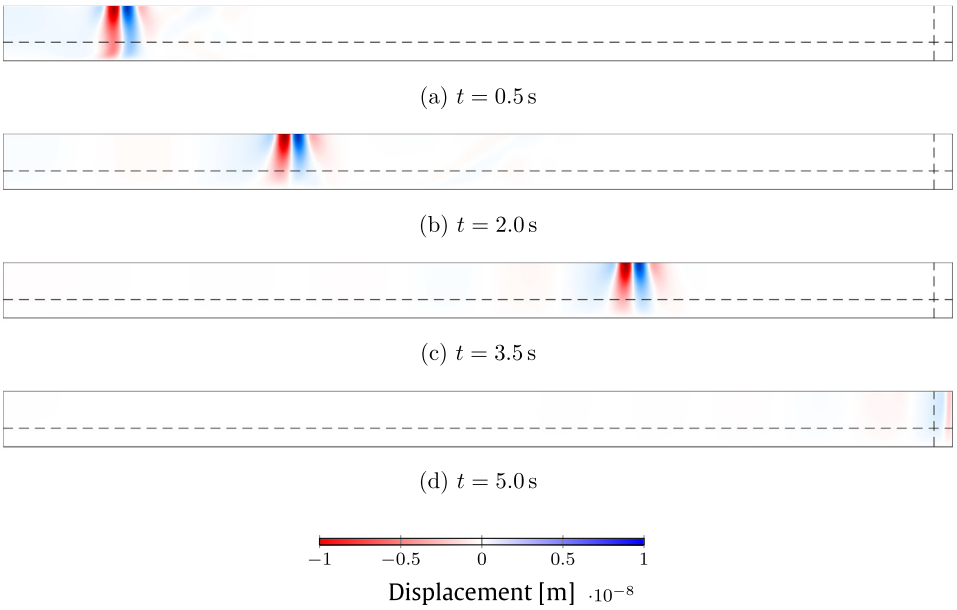

Fig. 12. Wavefield snapshots in a shallow elastic domain terminated by a CFS-PML buffer ($\omega_0 = 5\pi$ rad/s): (a) $t = 0.5$ s, (b) $t = 2.0$ s, (c) $t = 3.5$ s, and (d) $t = 5.0$ s.

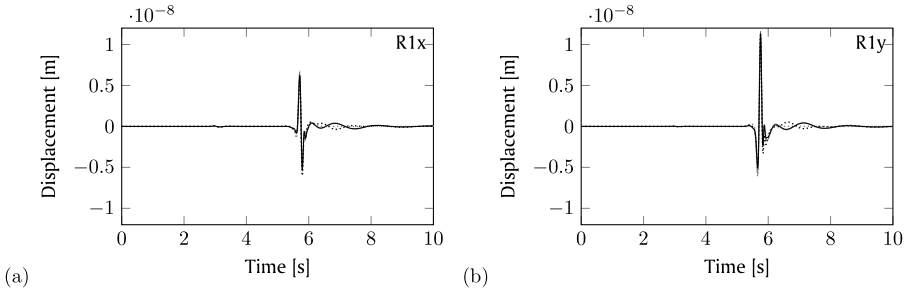

Fig. 13. Time history of: (a) horizontal; and (b) vertical displacement components at receiver R1 in a shallow elastic domain terminated by a standard PML buffer ($\omega_0 = 0$). The results are shown for the Q41 (solid gray), Q44 (dotted gray), Q81 (solid black), and Q84 (dotted black) elements.

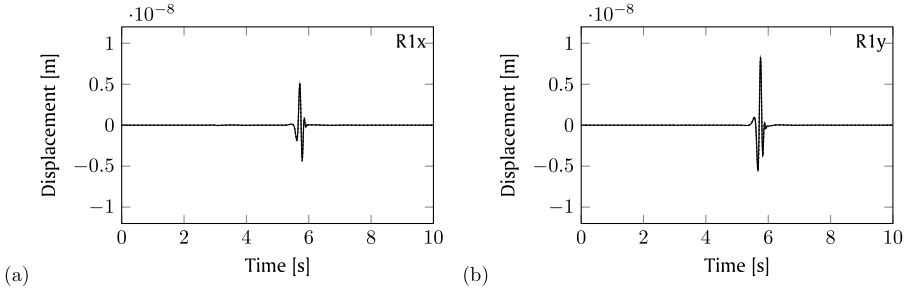

Fig. 14. Time history of: (a) horizontal; and (b) vertical displacement components at receiver R1 in a shallow elastic domain terminated by a CFS-PML buffer ($\omega_0 = 5\pi$ rad/s). The results are shown for the Q41 (solid gray), Q44 (dotted gray), Q81 (solid black), and Q84 (dotted black) elements.

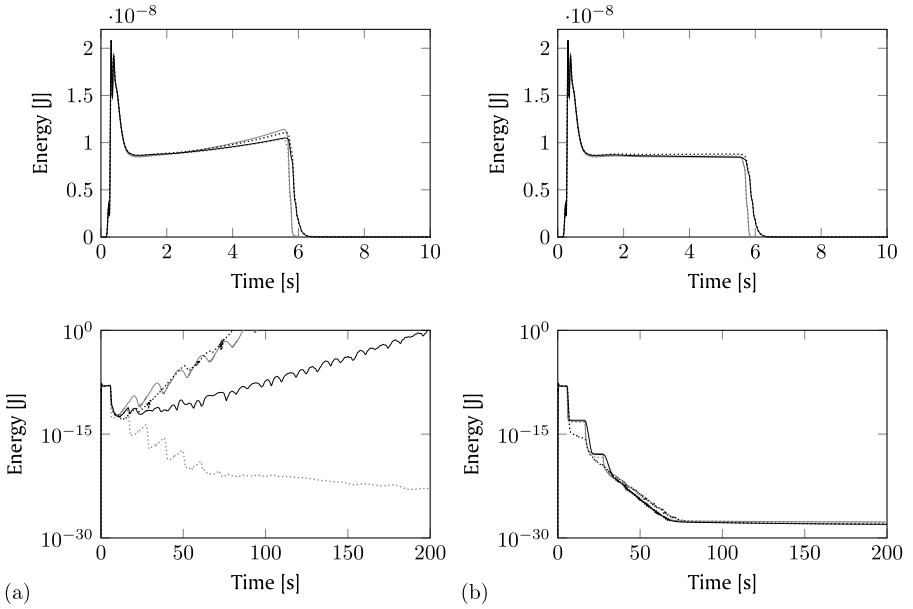

Fig. 15. Energy in the interior of the shallow domain (case 2) for: (a) standard PML ($\omega_0 = 0$); and (b) CFS-PML ($\omega_0 = 5\pi$ rad/s). Results are shown for the Q41 (solid gray), Q44 (dotted gray), Q81 (solid black), and Q84 (dotted black) elements. The results are plotted on a linear scale for $0 \le t \le 10$ s (top row), and on a logarithmic scale for $0 \le t \le 200$ s (second row).

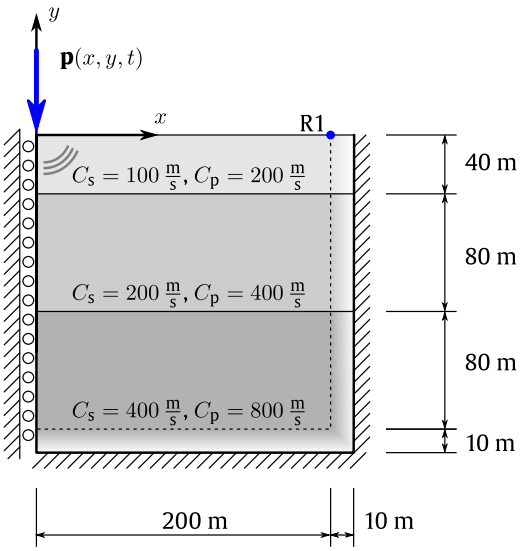

Fig. 16. PML-truncated semi-infinite layered medium.

for the top layer, $C_s = 200\,\frac{m}{s}$ for the second layer, and $C_s = 400\,\frac{m}{s}$ for the underlying halfspace. The Poisson ratio $\nu = \frac{1}{3}$ and the mass density $\rho = 1800\,\frac{kg}{m^3}$ are assumed constant for the layers and the halfspace. Furthermore, we consider the same Ricker pulse loading as in the preceding cases (Eq. (66)), and the same mesh and time-integration scheme as those used for the case 1 experiment.

Fig. 17 depicts wavefield snapshots of the vertical displacement component at various times, where the reflections from the layer interfaces create a complicated wave pattern. Fig. 18 shows the corresponding time histories of the horizontal and vertical displacement components at receiver R1. Despite the complexity, both the standard PML and the CFS-PML result in a similarly effective absorption of the elastic waves at early times. However, as shown in

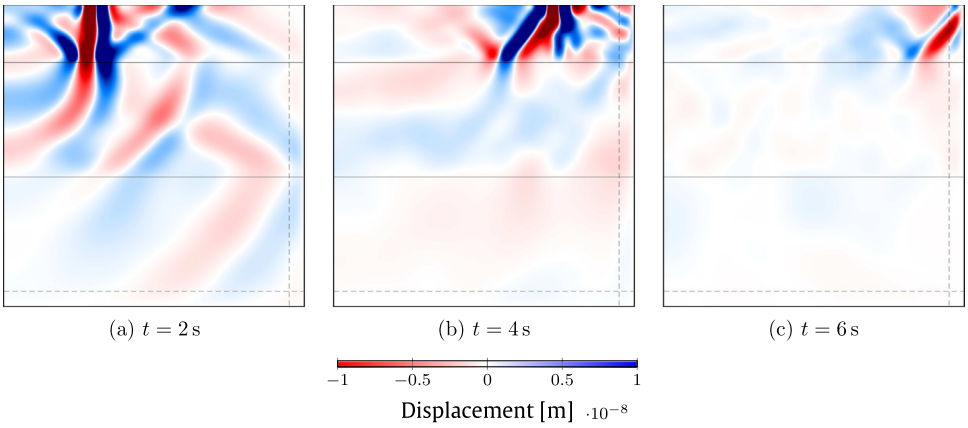

Fig. 17. Wavefield snapshots of the vertical displacement component in a layered elastic medium terminated by a CFS-PML buffer with $\omega_0 = 5\pi$ rad/s: (a) $t = 2$ s; (b) $t = 4$ s; and (c) $t = 6$ s.

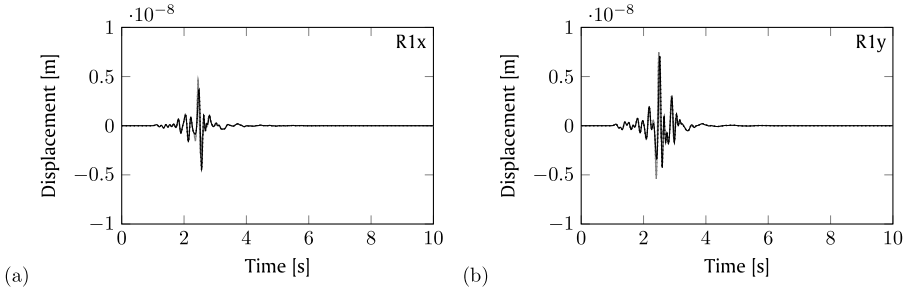

Fig. 18. Time history of: (a) horizontal; and (b) vertical displacement components at receiver R1 in a layered elastic medium terminated by a CFS-PML buffer with $\omega_0 = 5\pi$ rad/s. The results are shown for the Q41 (solid gray), Q44 (dotted gray), Q81 (solid black), and Q84 (dotted black) elements.

Fig. 19 (bottom left), among the standard PML elements, it is now the Q84 that exhibits exponential error growth. By contrast all of the new CFS-PML elements, including the Q84, appear to be stable, as shown in Fig. 19 (bottom right).

6. Conclusions

In this paper we discussed a new non-convolutional, second-order, unsplit-field, finite element formulation of the CFS-PML. The desirable second-order temporal character of the resulting formulation was achieved through the introduction of auxiliary fields, local to the PML buffer only. Using low-order polynomial approximations for the displacement components and the auxiliary fields, we derived the first four members of a family of CFS-PML elements that are fully defined by a triad of element stiffness, damping, and mass matrices, which could be readily incorporated into existing codes.

The performance of the proposed multi-field CFS-PML elements was numerically tested in homogeneous and heterogeneous domains, including layered and arbitrarily heterogeneous media: a subset of these experiments was presented herein to demonstrate the relative performance of the various CFS-PML elements, and to compare their performance against the standard PML. While both the PML and CFS-PML force the rapid and effective wave decay within the PML buffer, the standard PML is plagued by long-time instability, even for isotropic, homogeneous media. To date, the standard PML's instability can be delayed through judicious parameterization of the PML, but cannot be completely eliminated; by contrast, the CFS-PML, using any of the four developed elements, appears to result in stable long-time behavior.

The low-order interpolation of the auxiliary fields of the Q41 and Q81 CFS-PML elements entails only a small error compared to its higher-order counterparts (Q44 and Q84, respectively), while significantly reducing the number

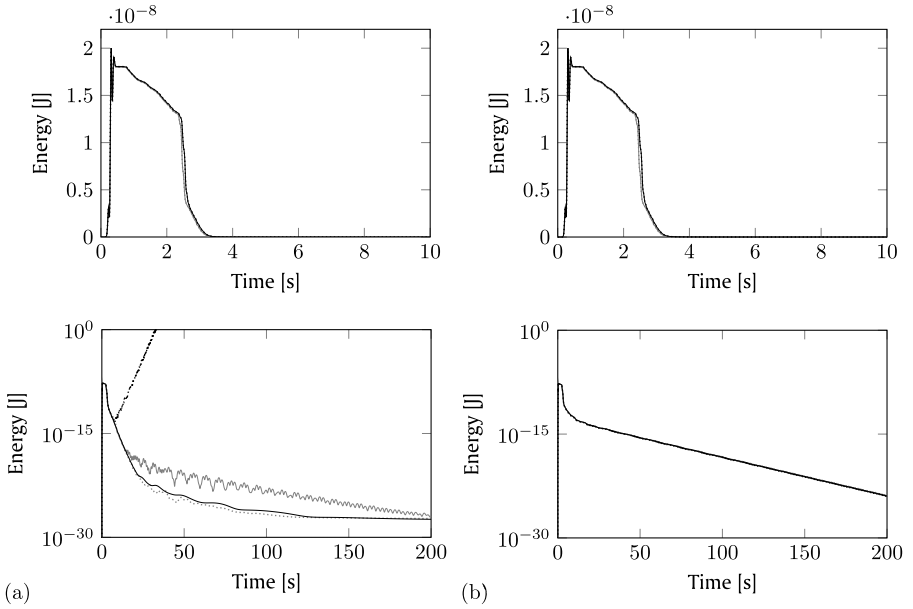

Fig. 19. Energy in the interior of the layered medium (case 3) for: (a) standard PML ($\omega_0 = 0$); and (b) CFS-PML ($\omega_0 = 5\pi$ rad/s). Results are shown for the Q41 (solid gray), Q44 (dotted gray), Q81 (solid black), and Q84 (dotted black) elements. The results are plotted on a linear scale for $0 \leq t \leq 10$ s (top row), and on a logarithmic scale for $0 \leq t \leq 200$ s (second row).

of degrees-of-freedom: for a typical mesh, the new CFS-PML Q81 element only doubles the number of degrees-of-freedom with respect to an elastic Q8 element, while providing the needed wave attenuation within the PML buffer. In summary, the new CFS-PML formulation and associated elements offer an efficient and robust scheme for numerically modeling transient elastic wave propagation in arbitrarily heterogeneous unbounded domains, while also retaining the second-order character of the elastic wave equations.

Declaration of competing interest

The authors declare that they have no known competing financial interests or personal relationships that could have appeared to influence the work reported in this paper.

References

[1] A. Sommerfeld, Die greensche funktion der schwingungsgleichung, Jahresber. Dtsch. Math.-Ver. 21 (1912) 309–353.
[2] V.D. Kupradze, On Sommerfeld's radiation principle, Dokl. Akad. Nauk SSSR 1 (2) (1934) 52–58.
[3] V.D. Kupradze, Three-Dimensional Problems of the Mathematical Theory of Elasticity and Thermoelasticity, North-Holland, Amsterdam, 1979.
[4] D. Beskos, T. Krauthammer, I. Vardoulakis (Eds.), Dynamic Soil–Structure Interaction, A.A. Balkema, 1984.
[5] J. Luco, H. Wong, Seismic response of foundations embedded in a layered half-space, Earthq. Eng. Struct. Dyn. 15 (1987) 233–247.
[6] M. Israeli, S.A. Orszag, Approximation of radiation boundary conditions, J. Comput. Phys. 41 (1) (1981) 115–135.
[7] J. Bérenger, A perfectly matched layer for the absorption of electromagnetic waves, J. Comput. Phys. 41 (1994) 115–135.
[8] W. Chew, W. Weedon, A 3D perfectly matched medium from modified Maxwell's equations with stretched coordinates, Microw. Opt. Technol. Lett. 7 (13) (1996) 599–604.
[9] E. Kausel, J.M. de Oliveira Barbosa, PMLs: A direct approach, Internat. J. Numer. Methods Engrg. 90 (3) (2012) 343–352, http://dx.doi.org/10.1002/nme.3322.
[10] E. Kausel, Personal communication with the third author.
[11] W. Chew, Q. Liu, Perfectly matched layers for elastodynamics: A new absorbing boundary condition, J. Comput. Acoust. 4 (4) (1996) 341–359.
[12] U. Basu, A. Chopra, Perfectly matched layers for time-harmonic elastodynamics of unbounded domains: theory and finite-element implementation, Comput. Methods Appl. Mech. Engrg. 192 (11–12) (2003) 1337–1375.
[13] U. Basu, A. Chopra, Perfectly matched layers for transient elastodynamics of unbounded domains, Internat. J. Numer. Methods Engrg. 59 (2004) 1039–1045.

[14] U. Basu, A. Chopra, Erratum to "perfectly matched layers for transient elastodynamics of unbounded domains", Internat. J. Numer. Methods Engrg. 61 (2004) 156–157.
[15] U. Basu, Explicit finite element perfectly matched layer for transient three-dimensional elastic waves, Internat. J. Numer. Methods Engrg. 77 (2009) 151–176.
[16] S. Kucukcoban, L. Kallivokas, Mixed perfectly-matched-layers for direct transient analysis in 2D elastic heterogeneous media, Comput. Methods Appl. Mech. Engrg. 200 (1–4) (2011) 57–76.
[17] S. Kucukcoban, L. Kallivokas, A symmetric hybrid formulation for transient wave simulations in PML-truncated heterogeneous media, Wave Motion 50 (1) (2013) 57–79.
[18] A. Fathi, B. Poursartip, L.F. Kallivokas, Time-domain hybrid formulations for wave simulations in three-dimensional PML-truncated heterogeneous media, Internat. J. Numer. Methods Engrg. 101 (3) (2015) 165–198.
[19] M. Poul, A. Zerva, Time-domain PML formulation for modeling viscoelastic waves with Rayleigh-type damping in an unbounded domain: Theory and application in ABAQUS, Finite Elem. Anal. Des. 152 (2018) 1–16.
[20] W. Zhang, E.E. Seylabi, E. Taciroglu, An ABAQUS toolbox for soil–structure interaction analysis, Comput. Geotech. 114 (2019) 103143.
[21] G. Festa, J.-P. Vilotte, The newmark scheme as velocity-stress time-staggering: an efficient PML implementation for spectral element simulations of elastodynamics, Geophys. J. Int. 161 (2005) 789–812.
[22] G. Festa, E. Delavaud, J.-P. Vilotte, Interaction between surface waves and absorbing boundaries for wave propagation in geological basins: 2D numerical simulations, Geophys. Res. Lett. 32 (L20306) (2005) 1–4.
[23] J.-F. Semblat, A. Pecker, Waves and Vibrations in Soils: Earthquakes, Traffic, Shocks, Construction Works, IUSS Press, Pavia, 2009.
[24] M. Kuzuoglu, R. Mittra, Frequency dependence of the constitutive parameters of causal perfectly matched anisotropic absorbers, IEEE Microw. Guid. Wave Lett. 6 (12) (1996) 447–449.
[25] D. Komatitsch, R. Martin, An unsplit convolutional perfectly matched layer improved at grazing incidence for the seismic wave equation, Geophysics 72 (5) (2007) 155–167.
[26] R. Martin, D. Komatitsch, S.D. Gedney, A variational formulation of a stabilized unsplit convolutional perfectly matched layer for the isotropic or anisotropic seismic wave equation, Comput. Model. Eng. Sci. 37 (3) (2008) 274–304.
[27] R. Matzen, An efficient finite element time-domain formulation for the elastic second-order wave equation: A non-split complex frequency shifted convolutional PML, Internat. J. Numer. Methods Engrg. 88 (10) (2011) 951–973.
[28] Z. Xie, D. Komatitsch, R. Martin, R. Matzen, Improved forward wave propagation and adjoint-based sensitivity kernel calculations using a numerically stable finite-element PML, Geophys. J. Int. 198 (3) (2014) 1714–1747.
[29] M. Zhuang, Q. Zhan, J. Zhou, Z. Guo, N. Liu, Q.H. Liu, A simple implementation of PML for second-order elastic wave equations, Comput. Phys. Comm. 246 (2020) 106867.
[30] S.A. Cummer, A simple nearly perfectly matched layer for general electromagnetic media, IEEE Microw. Wirel. Compon. Lett. 13 (3) (2003) 128–130.
[31] K. Meza-Fajardo, A. Papageorgiou, A nonconvolutional, split-field, perfectly matched layer for wave propagation in isotropic and anisotropic elastic media: Stability analysis, Bull. Seismol. Soc. Am. 98 (4) (2008) 1811–1836.
[32] W. Chew, J. Jin, E. Michielssen, Complex coordinate stretching as a generalized absorbing boundary condition, Microw. Opt. Technol. Lett. 15 (6) (1997) 363–369.
[33] J.-P. Bérenger, Application of the CFS PML to the absorption of evanescent waves in waveguides, IEEE Microw. Wirel. Compon. Lett. 12 (6) (2002) 218–220.
[34] J.A. Roden, S.D. Gedney, Convolution PML (CPML): An efficient FDTD implementation of the CFS–PML for arbitrary media, Microw. Opt. Technol. Lett. 27 (5) (2000) 334–339.
[35] K. Bathe, Finite Element Procedures, second ed., Prentice-Hall, Englewood Cliffs, NJ, 1996.
[36] R. Cook, Finite Element Modelling for Stress Analysis, John Wiley and Sons, 1995.
[37] R. Cook, D. Malkus, M. Plesha, R. Witt, Concepts and Applications of Finite Element Analysis, fourth ed., John Wiley and Sons, 2002.
[38] O.C. Zienkiewicz, R.L. Taylor, The Finite Element Method for Solid and Structural Mechanics, Elsevier, 2005.
[39] T.J. Hughes, The Finite Element Method: Linear Static and Dynamic Finite Element Analysis, Courier Corporation, 2012.
[40] T. Belytschko, J.S.-J. Ong, W.K. Liu, J.M. Kennedy, Hourglass control in linear and nonlinear problems, Comput. Methods Appl. Mech. Engrg. 43 (3) (1984) 251–276.
[41] T. Belytschko, W.K. Liu, B. Moran, K. Elkhodary, Nonlinear Finite Elements for Continua and Structures, John wiley & Sons, 2013.
[42] E. Wilson, R. Taylor, W. Doherty, J. Ghaboussi, Incompatible displacement models, in: Numerical and Computer Methods in Structural Mechanics, Elsevier, 1973, pp. 43–57.
[43] R.L. Taylor, P.J. Beresford, E.L. Wilson, A non-conforming element for stress analysis, Internat. J. Numer. Methods Engrg. 10 (6) (1976) 1211–1219.